

1 **Vapor-deposited minerals contributed to the martian surface during degassing of Cl- and**
2 **S-bearing, OH-poor lava**

3 **H. Nekvasil¹, N. J. DiFrancesco², A. D. Rogers¹, and P. L. King³**

4 ¹Stony Brook University, Department of Geosciences, Stony Brook, NY 11790, USA

5 ²SUNY Oswego, Department of Atmospheric and Geological Sciences, Oswego, NY 13126,
6 USA

7 ¹Stony Brook University, Department of Geosciences, Stony Brook, NY 11790, USA

8 ³Research School of Earth Sciences, The Australian National University, Canberra, ACT 2601,
9 Australia

10 Corresponding author: Hanna Nekvasil (hanna.nekvasil@stonybrook.edu)

11 **Key Points:**

12 • Gas from Cl- and S-rich, OH-poor magma readily transports iron and alkalis.

13 • Magmatic gas produces micron-sized crystals of molysite, halite, sylvite, hematite,
14 maghemite, silica, pyrrhotite, pyrite and native sulfur.

15 • The surface deposits may react during cooling and hydration to produce secondary
16 phases including iron oxychlorides and hematite.

17

18 **Abstract**

19 Martian magmas were likely enriched in S and Cl with respect to H₂O. Exsolution of a vapor
20 phase from these magmas and ascent of the gas bubbles through the magma plumbing system
21 would have given rise to shallow magmas that were gas-charged. Release and cooling of this gas
22 from lava flows during eruption may have resulted in the addition of a significant amount of
23 vapor-deposited phases to the fines of the surface. Experiments were conducted to simulate
24 degassing of gas-charged lava flows in order to determine the nature of vapor-deposited phases

25 that may form through this process. The results indicate that magmatic gas may have contributed
26 a large amount of Fe, S, and Cl to the martian surface through the deposition of iron oxides
27 (magnetite, maghemite, hematite), chlorides (molysite, halite, sylvite), sulfur and sulfides
28 (pyrrhotite, pyrite). Primary magmatic vapor-deposited minerals may react during cooling to
29 form a variety of secondary products, including iron oxychloride (FeOCl), akaganéite
30 ($\text{Fe}^{3+}\text{O(OH,Cl)}$), and jarosite ($\text{KFe}^{3+}_3(\text{OH})_6(\text{SO}_4)_2$). Vapor-deposition does not transport
31 significant amounts of Ca, Al, or Mg from the magma and hence, this process does not directly
32 deposit Ca- or Mg sulfates.

33

34 **1 Introduction**

35 **1.1 Occurrence of S and Cl on the Martian Surface**

36 Chlorine and sulfur have been recognized as major components of martian surface
37 materials since Viking lander measurements of the regolith (e.g., Baird et al., 1976; Clark &
38 Baird, 1979; Clark et al., 1977; 1982). Subsequent rovers with the Pathfinder, the Mars
39 Exploration Rover (MER), and Mars Science Laboratory (MSL) missions and the Phoenix lander
40 confirmed these observations (reviews in King and McLennan, 2010; Galliard et al., 2013; Franz
41 et al., 2019), even noting veins of sulfur-rich material containing up to 40 wt.% S (Nachon et al.,
42 2014). In-situ measurements of the regolith by the instrument suites on board the MSL and MER
43 rovers plus remote infrared and gamma ray spectra from orbit suggest that sulfur is specifically
44 hosted by Mg-, Fe- and Ca-sulfates (such as anhydrite), as well as pyrite, pyrrhotite, jarosite, and
45 minor amounts of other sulfates, sulfides, and native sulfur (review in Franz et al., 2019).

46 Orbiter data suggest that the Cl concentration of the martian surface ranges from
47 approximately 0.1 to 1 wt% with an average of 0.49 wt% globally (Keller et al., 2006). Elevated
48 chlorine concentrations of the martian surface have also been confirmed by all rover and lander
49 missions (Clark & van Hart, 1981; Gellert et al., 2004; 2006; Hecht et al., 2009; McLennan et al.,
50 2014; Wanke et al., 2001). The Cl content of martian dust and soil compositions from the Alpha-
51 particle X-ray Spectrometer (APXS) and mass spectrometry using the Sample Analysis at Mars
52 (SAM) instrument (Berger et al., 2016; Glavin et al., 2013) are in general agreement with the
53 orbiter data. The abundant chlorine on Mars is hosted in reduced chlorides (Cl^-), and oxidized
54 perchlorates (Cl^{4+}) and chlorates (Cl^{5+}). THEMIS data indicate that Cl is in part hosted by halite
55 and possibly other chlorides such as sylvite and molysite in playa-like deposits on Mars
56 (Osterloo et al., 2008, 2010); for example, Glotch et al. (2016) suggest that halite may comprise
57 up to 25% of the fines in these regions. Chlorine is also hosted by perchlorate salts in the regolith
58 of Mars' North Pole investigated by the Phoenix Mars Lander (Hecht et al., 2009; Kounaves et
59 al., 2014) and in the Rocknest fines at Gale Crater by MSL (Glavin et al., 2013).

60 Commonly considered mechanisms for the formation of the sulfates and
61 chlorides/perchlorates in martian fine-grained material involve secondary processes acting upon
62 pre-existing sulfide- and chloride-bearing bedrock sources. Studies of igneous martian meteorites
63 indicate that these rocks contain primary igneous sulfides, predominantly pyrrhotite (see review
64 of King and McLennan, 2010), and Cl-bearing minerals, such as amphiboles (e.g., Johnson et al.,
65 1991) and apatite (e.g., McCubbin & Nekvasil, 2008; Righter et al., 2002). Oxidation of primary
66 sulfide minerals to form sulfates is speculated to have occurred through water-rock or ice-rock
67 interaction (Bibring et al., 2006; Burns & Fisher, 1990; Chevrier & Mathé, 2007; King et al.,
68 2004; King & McSween, 2005; McCollom & Hynek, 2005; Niles & Michalski, 2009; Yant et al.,

69 2016). Sulfate dispersion into martian fines would then have resulted from mechanical erosion of
70 these secondary sulfates, dissolution and possible transport in fluvial systems, followed by
71 evaporation of surface waters before aeolian transport. Martian chloride deposits are also
72 considered to be secondary in nature, with aqueous dissolution of Cl from an original chloride-
73 bearing bedrock followed by evaporation either in situ (Osterloo et al., 2008; 2010) or after
74 significant transport to lake beds and deltaic regions (e.g., Hynek et al., 2015).

75 Secondary processes such as alteration, erosion, and transport of bedrock sulfides and
76 chlorides undoubtedly remobilized Cl and S to the martian regolith. However, it has been long
77 recognized that magmatic gas also has a significant role in transporting S and halogens to the
78 surface (e.g., Banin et al., 1997; Clark & Van Hart, 1981; King and McSween, 2005; Settle,
79 1979; Ustunisik et al., 2011) and can produce both primary vapor-deposited minerals and
80 secondary minerals through interaction with the surface. While much effort has gone into
81 exploring sedimentological processes that contributed to the enrichment of these elements in
82 martian fines, less is known about the role of magmatic vapors in forming halogen- and sulfur-
83 bearing minerals (Gooding, 1978; Gooding et al., 1992).

84 **1.2 Contributions of magmatic gas to the martian surface**

85 On Earth, magmatic gas released during major explosive eruptions is considered to be a
86 primary contributor of H₂O, and C-, S and Cl-bearing gaseous species to the atmosphere. Large
87 explosive tephra-producing eruptions on Mars likely also primarily contributed gaseous species
88 such as H₂O, SO₂, HCl, S and H₂S to the atmosphere, with SO₂ dominating as a primary
89 magmatic gaseous species (Symonds et al., 1994; Gaillard & Scaillet, 2009) and as a secondary
90 species produced by reaction of H₂S in the martian atmosphere (e.g., Bluth et al., 1995). Such

91 large explosive eruptions are commonly called upon to account for widespread aerosol sulfate
92 production through both wet and dry processes on Earth and on Mars (e.g., Settle, 1979).
93 However, persistent quiescent degassing from lava flows, small scale fire-fountaining, shallow
94 magma bodies, and small fumaroles, commonly referred to as “open-vent” or “passive”
95 degassing, could have provided even more volcanic gas to the Martian surface over time than the
96 less common explosive events, as has been the case even for Earth (Mather et al., 2003).

97 Shallow degassing as a significant source of magmatic gas appears inconsistent with the
98 low volatile solubilities in low-pressure magma, as low volatile solubility would imply only an
99 insignificant amount of gas would be released by exsolution from a cooling lava flow. However,
100 it has been proposed that gas from deeper portions of the magma plumbing can become
101 concentrated in shallow regions - a process invoked to explain the “excess S” problem on Earth
102 (Wallace 2001) - and loss of this entrained gas during quiescent volcanism would contribute
103 more magmatic gas to the martian surface than could be provided solely by low pressure
104 exsolution of gas from the erupted lava. This process has also been called upon to concentrate
105 H₂O-CO₂-Cl-S-bearing gases (e.g., Johnson et al., 2010). Localized degassing and cooling of the
106 gas released from passive magmatism would result in a smaller contribution of magmatic gas to
107 the upper atmosphere and larger contribution to the local surface through the formation of vapor-
108 deposited solids.

109 Our understanding of the nature of volcanic gas sublimes and their stability temperatures
110 has been greatly aided by direct observation of sublimate production on Earth. Silica glass tubes
111 positioned inside small fumaroles allow for the concentration of vapor and the collection of
112 precipitated mineral phases forming along the inner walls of the tube (e.g., Africano et al., 2002;
113 Bernard & Le Guern, 1986; Taran et al., 1995; Yudovskaya et al., 2008; Zelenski et al., 2013).

114 Analysis of sublimates forming from gas emitted at high temperature vents from the potential
115 martian analog shield volcano Erte Ale (on the East African rift, Benoit et al., 2006; de Moor et
116 al., 2013) shows a high-to-low temperature sequence of oxides, silicates, platinum group
117 elements, sulfides, sulfates, halides, fluorosilicates and native sulfur (Zelenski et al., 2013). The
118 most abundant sublimate minerals observed were Fe/Ti oxides, silicates, halite, sylvite,
119 amorphous silica, native sulfur and trace metal-sulfides/chlorides (Zelenski et al., 2013).

120 It is not known how well terrestrial magmatic vapor-deposited material reflects the vapor-
121 deposited minerals produced on Mars during passive degassing, since the compositions of
122 volcanic gas and the subsequently vapor-deposited minerals are dependent on the composition
123 and the volatile load of the parental magma/lava from which the gases were exsolved (e.g.,
124 Renggli et al., 2017). The possibility of significant differences between the dissolved volatile
125 load of martian magmas and terrestrial magmas has been recognized. S-bearing gaseous species
126 may have been more abundant in martian volcanic gases due to a higher S content of the martian
127 mantle. In fact, Gaillard & Scaillet (2009) concluded that up to 50 mol% of the post 4.5 Ga
128 martian volcanic gases could have been composed of S-species. A lower water content of the
129 martian mantle and primary melts has been suggested based on petrologic evidence (e.g.,
130 Filiberto et al., 2016a; b; Kiefer et al., 2015; McCubbin et al., 2016). Also, Filiberto et al. (2016b
131 and references within) suggested that halogen concentrations in the martian mantle were as much
132 as three times greater than what is found in the terrestrial mantle. Adding to the potential of
133 significantly higher Cl/H₂O ratios of primitive martian magmas compared to primary terrestrial
134 magmas, is the expected mantle dehydration induced by successive partial melting of rising
135 mantle.

136 In view of the strong possibility that terrestrial fumarolic gases may not be analogous to
137 low-OH martian magmatic gases, the use of thermodynamic models of vapor/sublimate mineral
138 equilibria is a reasonable first-line approach to assessing the nature of martian vapor-deposited
139 mineral since they allow for compositional variability of the bulk gas composition. Model
140 prediction of such equilibria based on thermodynamic properties of a variety of species from
141 databases such as GASTHERM (Symonds & Reed, 1993) and JANAF (Chase, 1998) has
142 evolved from the early work by Krauskopf (1957). A variety of software tools have been
143 developed that incorporate an increasing number of chemical species in the vapor (e.g., HSC
144 Chemistry by Outotec). As summarized by Pokrovski et al. (2013), these calculations have had
145 varied success in predicting sublimate chemistry of natural systems when compared to fumarole
146 analysis in silica glass tubes. Three problems with such comparisons can be readily envisioned.
147 First, the bulk gas composition, needed for any thermodynamic modeling, is a property that
148 remains elusive in many natural fumaroles; this is even more the case for Mars. Second,
149 equilibrium thermodynamics may not be applicable in a regime of high thermal gradient such as
150 above a lava flow (e.g., Patrick et al., 2004), where thermodiffusion (Soret diffusion) can induce
151 heterogeneous gas compositions over this gradient even for an originally homogeneous vapor.
152 Finally, degassing lava flows or shallow magma bodies have a dispersed gas source (the lava
153 itself) and during cooling, superposition of high and low temperature phases can be expected to
154 occur across the surface of a flow. Importantly, this superposition will allow for reaction among
155 previously precipitated phases during cooling that may lead to the formation of secondary
156 minerals not predicted by thermodynamic sublimation modeling. For these reasons, we have
157 elected to follow an experimental approach towards investigating the nature of vapor deposited

158 material that could have been added to the Martian surface by passive degassing of OH-poor
159 magma.

160 **2 Experimental design**

161 Experiments attempt to simulate the natural cooling of magmatic gas proximal to a lava
162 flow or in a small fire fountain, a gas whose multi-component composition is initially dictated by
163 the magma it was in equilibrium with and then modified due to thermodiffusion and precipitation
164 of vapor-deposited minerals. Furthermore, these experiments were designed to emulate the
165 mixing of high and low temperature vapor-deposited phases and the reactions among them as the
166 local gas column cools.

167 The experiments were designed to (i) generate an oxidized magmatic froth that simulates
168 a gas bubble-charged shallow magma in which the gas has equilibrated with an oxidized crust,
169 (ii) allow this gas to separate from the silicate melt and ascend into an overlying cooler gas
170 column in a strong thermal gradient, (iii) enable the formation and collection of solid vapor-
171 deposited phases and (iv) cool the gas column in order to permit reaction among previously
172 precipitated phases.

173 The physical design of all experiments was modified from that of Ustunisik et al. (2011;
174 2015) and involved synthesis of a volatile-doped glass of basaltic composition (referred to here
175 as the vapor “source”) at elevated pressure (required to dissolve appropriate amounts of Cl and
176 S). This source was then placed in a crimped capsule (sealed at the bottom) at the bottom of a
177 long silica glass tube. The silica tube was evacuated, sealed, and placed in a vertically held
178 furnace such that the capsule was at the hotspot and below a strong thermal gradient. This setup
179 allowed the volatile-oversaturated source to melt and boil at low pressure, producing a high gas

180 to melt ratio, forcing the gas out of the crimped capsule and into the tube. The vapor was trapped
181 in the glass tube which allowed deposits to form as the gas cooled in the thermal gradient of the
182 overlying column (Fig. 1). In many ways, these experiments simulate the glass tube fumarolic
183 gas sampling technique used by workers such as Zelenski et al. (2013).

184 Assessment of the experimental technique was aided by additional experiments designed
185 to provide ground state information on whether crystalline vapor-deposited phases would form in
186 the absence of Cl and S, determine if the temperature of the source and hence the degree of
187 crystallinity affected the compositional types of vapor deposited phases produced, determine if
188 the structural state of the source played a significant role in determining the nature of the vapor-
189 deposited minerals produced, and whether the redox state of the source at the hotspot changed
190 during the experiment.

191 **2.1 Source material composition**

192 Considering the likelihood that source composition plays a role in the nature of vapor
193 deposited minerals produced, a martian rock composition, specifically, the APXS-analyzed
194 composition of the Gusev Crater rock “Irvine” (McSween et al., 2006), was chosen to provide
195 the magmatic froth. Irvine, a member of the Irvine-class rocks, was discovered in the Columbia
196 Hills of Gusev Crater in a small sub-linear outcrop, suggestive of an igneous dike. It has an
197 aphanitic texture indicative of rapid crystallization and thus, is likely an igneous rock that has
198 retained the composition of the magma from which it formed. Mini-TES and Mössbauer data
199 indicate a modal mineralogy consisting of predominantly feldspar and pyroxene, Fe-Ti-oxides,
200 as well as minor olivine and apatite (McSween et al., 2006), that is, a typical basaltic assemblage
201 with little alteration (Morris et al., 2006). Chemical analysis showed that Irvine is a mildly

202 alkalic basalt (McSween et al., 2006) with a composition similar to the bulk martian crust (Hahn
203 & McLennan, 2010). The Irvine composition contains both S and Cl. Although much of this is
204 attributed to contamination by surface dust (McSween et al., 2006), it should be noted that the S
205 content reported for this unbrushed rock (2.4 wt% SO_3 or 1 wt% S) is not an unreasonable S
206 content of an oxidized basalt at sulfide saturation (Jugo et al., 2010).

207 **2.2 Volatile load**

208 In order to ensure a high gas content for the experiment, a high gas/silicate melt ratio in
209 the magmatic froth was required. Towards this end, the source synthesis capitalized on the higher
210 volatile solubility at higher pressure. The Irvine composition synthesized was doped with S and
211 Cl to levels higher than their likely magma concentrations at low pressure. This was purely to
212 produce a source glass that was supersaturated in volatiles at low pressure. This supersaturation
213 enabled the source to boil at low pressure and form the froth, thus simulating the magmatic froth
214 produced by gas bubble concentration in the shallow reaches of a magma plumbing system.
215 Whether the gas was concentrated in nature by ascent into shallow reaches of the magma
216 plumbing system, or exsolved due to supersaturation at low pressure as is the case for the
217 experiments, the final gas would be in equilibrium with the low-pressure silicate melt.

218 Using as a starting point the bulk chemical composition of the “soil-corrected” Irvine
219 where the majority of S and Cl was computationally removed (McSween et al., 2006), the effect
220 of volatile ratio, specifically S/Cl, was investigated by synthesizing two volatile-bearing
221 compositions in addition to a Cl- and S-free composition (listed in Table 1 as no volatiles added
222 “NVA” experiments). The presence of both Cl and S in each of the halogen-bearing source
223 compositions ensured that the expected competition for coordinating ligands between the two

224 anions was preserved. Based on the S solubility inferred by Gaillard & Scaillet (2009), the high S
225 composition synthesized was anticipated to exsolve an immiscible sulfide liquid during high
226 pressure synthesis which would crystallize during quench. Inclusion of this sulfide phase with
227 the silicate glass as the source ensured a higher S budget of the source than the glass alone. The
228 concentration of Cl for our Cl-bearing sources is ~3-5 times greater than observed in Irvine,
229 again with the goal of producing a sufficient amount of gas-charged silicate froth and simulating
230 a gas+ silicate melt assemblage at low pressure that is enriched in gas from bubble ascent.
231 Although natural systems can concentrate a large amount of gas, we were limited by the
232 solubility of Cl at our synthesis pressure in the ratio of gas to melt at low pressure that we could
233 produce.

234 **2.3 Redox State**

235 The oxygen fugacity of the source material will affect the nature of the vapor-deposited
236 minerals produced and, therefore, deserves special consideration in the experimental design. In
237 spite of its apparent lack of alteration, the rock Irvine has a $\text{Fe}^{3+}/\Sigma\text{Fe}$ of 0.36, as determined
238 though Mössbauer spectroscopy and estimates of igneous mineral composition (Schmidt et al.,
239 2013). This high degree of oxidation has been attributed at least in part to the oxidized dust layer
240 (McSween et al., 1994). However, Schmidt et al. (2013), in their re-evaluation of the oxygen
241 fugacities of the igneous minerals in several martian basalts, inferred oxygen fugacities for Irvine
242 near QFM. While this corresponds to a more oxidized state than was originally accepted for
243 martian basalts (e.g., Herd et al., 2001; 2006), a wide diversity of oxygen fugacities has been
244 reported for these basalts. Oxygen fugacity estimates range from values suggestive of IW to the
245 NNO buffer (Herd, 2006; McSween, 1994; Santos et al., 2015; Schmidt et al., 2013). Not all of
246 the higher oxidation states observed can be explained by weathering processes, suggesting they

247 may be magmatic (e.g., Santos et al., 2015). Herd (2001; 2006) and Wadhwa (2008) suggested
248 that some of this oxidation occurred in the magmatic state after exposure to, or mixing with,
249 more oxidized materials or magmas in the crust. This relatively high oxygen fugacity is similar
250 to values for the augite basalt/shergottite NWA 8159 (Herd et al., 2017) that began crystallizing
251 near or just below FMQ, with a later increase in oxygen fugacity to approximately 2 log units
252 above FMQ. Since (i) Irvine appears to show minerals consistent with FMQ or slightly higher
253 (Schmidt et al., 2013), (ii) there is clear evidence that martian magmas can become oxidized
254 when ascending to shallow levels, and (iii) oxidation of entrained gas should be readily attained
255 during exposure to oxidized crust, we have chosen to investigate degassing of a magma of Irvine
256 composition at an oxidation state intermediate between that of the magma and that of the surface,
257 specifically, close to the NNO buffer. In this way we can provide information on the oxidized
258 vapor deposited assemblage.

259 The late changes in oxygen fugacity in the igneous assemblage of some martian rocks
260 attests to the absence of an oxygen buffering assemblage in at least some martian magmas at
261 shallow levels. For this reason, the experiments were designed without an oxygen buffering
262 assemblage. Instead the ferrous/ferric ratio was set to be that of NNO at 1150°C in the starting
263 source material. The value of this initial ratio was obtained by using the Irvine composition for a
264 MELTS analysis (Ghiorso & Sack, 1995) of the effect of $\log (f\text{O}_2/1 \text{ bar})$ (that is, log fugacity of
265 oxygen relative to a 1 bar standard state) on the melt $\text{Fe}^{3+}/\text{Fe}^{2+}$ ratio.

266 Considering the uncertainty of the computational models employed (which led to the
267 computed ferric/ferrous ratio used), weighing uncertainty of the Fe sources, and potential for the
268 oxygen fugacity of the molten source to change during the experiment (e.g., through oxidation of
269 the melt caused by reduction of ferrous iron to Fe° in the melt and alloying of this metallic Fe to

270 the Au₈₀Pd₂₀ capsule), an independent measure of the oxygen fugacity at the source was desired.
271 To do this, we ran additional experiments that included a two-oxide oxygen monitor (Buddington
272 & Lindsley, 1964). For this monitoring, the compositions of a two-oxide pair (an ilmenite-
273 hematite solid solution and a ulvöspinel magnetite solid solution) in equilibrium at 1150°C at the
274 oxygen fugacity of the NNO buffer were computed using the thermodynamic model QUILF
275 (Andersen et al., 1993) and the value of the oxygen fugacity from the above MELTS analysis. A
276 further calculation yielded an oxide pair that lay at slightly more oxidizing conditions. By using
277 the “off-composition” pair, any compositional change would ascertain that the monitor was not
278 acting as a buffer, and the direction of compositional change would constrain the redox state of
279 the source while melted. This oxide pair was included in a separate capsule alongside the source-
280 bearing capsule at the hotspot for two experiments, one using the I(NVA) and the other the
281 I(Cl+S) source. To further enhance the possibility that the monitor did not act as a buffer, the
282 weight ratio of monitor oxide to source was minimized. These oxides were re-analyzed after the
283 experiments to determine if they changed composition during the experiment.

284 **2.4 Structural state of the source**

285 Ideally in the laboratory, magma could be rapidly decompressed from elevated pressure
286 to the low pressure of the degassing experiments while still in the molten state. In the absence of
287 this capability, the use of quenched glass is a common alternative. However, some volatile
288 compounds may be lost from the source glass during heating in the silica glass tube while the
289 temperature it is still below the glass transition temperature, that is, while in a thermal regime
290 where the structural state and likely the binding energy of the volatile species may differ from a
291 melt. In order to assess the sensitivity of the nature of the vapor-deposited minerals to loss of
292 vapor before melting, we ran several parallel experiments using the reagent mixture of oxide

293 components itself (e.g., the same mix that was used to synthesize the glass at high pressure). This
294 starting material most likely would lose volatiles sequentially (due to decomposition of
295 individual components of the mixture). If the vapor-deposited phases are the same for these very
296 different source types and bonding environments, it is likely that even though the loss of gas
297 from the glass before melting glass is possible, the experiments may still provide information on
298 vapor-deposited material produced directly by a cooling magma and we can be more confident
299 that the simulated degassing information can be applied to natural systems.

300 **3 Experimental details**

301 Powdered components (oxides, silicates, chlorides, and sulfate) of the source magma
302 were mixed together in ethanol and homogenized in automatic agate mortars for approximately 4
303 hours. Fe^o sponge (needed for combination with hematite to provide the desired ferrous/ferric
304 ratio) and MgCl₂ (for the chlorine-bearing sources) were added in the last hour to mitigate any
305 oxidation or dissolution of the components, respectively. The Fe²⁺/(Fe²⁺+Fe³⁺) ratio of this
306 mixture was determined by the MELTS (Ghiorso & Sack, 1995) analysis mentioned above. This
307 analysis indicated that a log (fO₂/1 bar) of -7 (~.2 log units above NNO) at 1150°C would be
308 achieved by setting the Fe²⁺/(Fe²⁺+Fe³⁺) ratio of the synthetic source mixture to 0.8. For the
309 I(Cl+S) mixture (Table 1), Cl and S were added as MgCl₂ and Mg(SO₄) (with the remaining Mg
310 added as periclase) to yield 2.5 wt % Cl, and 0.6 wt % SO₃ equivalent. The high-sulfur source
311 mixture (I(Cl+HiS) of Table 1) was produced by adding an additional amount of pyrite+Fe^o
312 (with troilite stoichiometry) to the I(Cl+S) mix. Importantly, the variable oxidation state of the S
313 added to the mixtures likely contributed little to the overall oxidation state of the mix, as the
314 quantities of the S-bearing materials used was much lower the total Fe in the system (for which

315 the redox state was set). The I(NVA) composition of Table 1 was made using only MgO
316 (periclase) as the Mg source.

317 The glass gas sources were produced by placing aliquots of the mix powder into Fe-
318 soaked platinum capsules. These capsules were made by lining Pt capsules with (0.03 mm thick)
319 Fe° foil and heating them to 1200°C in vacuum for 6 hours to allow the metals to alloy (with the
320 hope of minimizing Fe-loss from our sample during glass synthesis). The capsules were loaded
321 with the reagent mixture and then dried at 150°C in a vacuum oven for 12 hours, welded shut,
322 and inserted into a talc cell containing a graphite furnace. Mullite spacers above and below the
323 capsule ensured that it would be held at the hotspot in the pressure vessel. The assemblage was
324 placed in 3/4 inch pressure vessel and inserted into a piston-cylinder press. The source mixtures
325 were melted at 0.5 GPa, and 1300°C for three hours, after which the charge was rapidly
326 quenched (~500 °C/min). Quenching produced a homogenous silicate glass or a silicate glass +
327 quenched immiscible sulfide melt as determined by electron microprobe analysis performed at
328 the American Museum of Natural History using a Cameca SX-100 microprobe. A 10 µm spot
329 size, accelerating voltage 20kV, and beam current of 15 mA was employed, with an analysis
330 time of 20-30 seconds per element. The following minerals were used for standardization:
331 McKee jadeite, Na; potassium feldspar, K; San Carlos olivine, Mg; Wakefield plagioclase, Si
332 and Ca; apatite, P; barite, S; Scapolite, Cl; ilmenite, Ti; MgCr₂O₄, Cr; rhodonite, Mn; Rockport
333 fayalite, Fe. Table 1 gives the electron microprobe analyses of the synthetic glass. Micro-FTIR
334 analysis of water content using the techniques of Dixon et al. (1995) and Mandeville et al. (2002)
335 indicate that the source glasses additionally contained 0.4_−0.2 wt% water; this uncertainty
336 reflects the combination of the uncertainty induced by thickness variation of individual glass
337 wafers and the overall variability of different aliquots of glass.

338 For the degassing experiments, the source glass (~150 mg) was loaded into Au₈₀Pd₂₀
339 capsules that were then loosely crimped and placed at the bottom of a ~28 cm long silica glass
340 tube (with a 7mm inner diameter), that was sealed at the bottom. The tube was evacuated, sealed
341 (by heating the open end with an oxygen torch while the tube was still attached to the vacuum
342 pump), and suspended in a vertical Pt-wound furnace with a thermal gradient such that the
343 sample was in the hotspot and the lowest temperature of the tube was at ~200°C. Insertion of the
344 tube was done over 20 minutes into the pre-heated furnace and the temperature of the hotspot
345 was rapidly re-attained once the tube was fully inserted. For the parallel experiments
346 investigating the effect of directly using the reagent mixture on the nature of the vapor-deposited
347 material, mixes were loaded into an Au₈₀Pd₂₀ capsule, and dried in a vacuum oven at 150°C for
348 12 hours before inserting into a silica glass tube and run under the same conditions as the glass
349 source. For each experiment the tubes were heated for between 12 and 96 hours with the source
350 at 1150° or 1200°C. Quenching involved removing the tube from the furnace and hanging it,
351 thereby allowing the tube to cool to room temperature.

352 For the experiments containing a 2-oxide oxygen monitor, the oxide pair used, with
353 nominal composition, Ilm₇₀Hm₃₀ and Usp₅₀Mt₅₀ (kindly donated by D.H. Lindsley), was
354 computed to reflect an oxygen fugacity of NNO+0.6 log units, that is 0.6 log units above what
355 was computed for our Fe²⁺/(Fe²⁺+Fe³⁺) ratio of 0.8. The oxide pair was powdered, mixed in a 1:1
356 ratio, and x-rayed (to verify the compositions using the cell parameters and the variation of cell
357 dimensions with changing composition of the solid solutions of Lindsley, 1976). This analysis
358 suggested that before experimentation the monitor pair consisted of Ilm₇₂Hm₂₈ and Usp₄₈Mt₅₂;
359 this composition, rather than the nominal composition, was used for comparison with the
360 monitor after exposure to gas. In order to minimize the chances that the monitor assemblage

361 itself acted as a buffer, the amount of the oxide monitor loaded was about 0.2 times that of the
362 source. [Although less monitor would be desirable, we had to ensure that sufficient monitor
363 would be present for a definitive powder XRD pattern of the oxide mixture after the experiment.]
364 The oxide mixture was loaded into an Au₈₀Pd₂₀ capsule which was placed adjacent to the source
365 container (and therefore, at the same temperature) inside the silica glass tube. The tube was then
366 inserted into the furnace identical in manner to other experiments. The experiments containing an
367 oxygen monitor were run for the same duration and quenched using the same technique as the
368 monitor-absent experiments.

369 In recognition that gas exsolution is a time-dependent process, the duration of the
370 experiments was varied from 12 to 96 hours in order to determine if there was a change in vapor
371 deposited assemblage. Likewise, in recognition of a thermal effect on diffusion, the temperature
372 of the source was changed. However, experimental technique limitations impeded our capability
373 to explore this to any significant extent. The upper temperature limit of the experimental
374 equipment used was 1200°C. Although the lower temperature limit (which is the S- and Cl-free
375 low-pressure solidus temperature) could be readily attained, the rise in solidus temperature
376 during degassing caused so much crystallization below 1150°C that the degassing melt was
377 continuously changing composition. This added an uncontrolled compositional variable that we
378 wished to avoid. For this reason, the difference in the hotspot temperature of successive
379 experiments was only 50°C and likely uninformative.

380 **4 Results**

381 Each silica glass tube was carefully inspected before opening. A variety of experiments
382 were deemed failures based on this observation and discarded. In some cases, the Au₈₀Pd₂₀

383 capsule had corroded and the sample had contacted the glass tube. In other cases, the source
384 magma had boiled over and escaped its capsule, pooling at the bottom of the silica glass, causing
385 it to rupture, sometimes explosively. Any tube that showed cracks, even those for which rupture
386 occurred during cooling (as observed in real time), was discarded. Every intact tube with a Cl-
387 and S-bearing source showed rings of coatings visible to the naked eye (Figs. 2, 3). Coatings
388 were not seen using the Cl- and S-free I(NVA) composition. The intact glass tubes remained
389 sealed and stored at room temperature until they were to be analyzed. Table 2 lists the successful
390 experiments.

391 Tubes from successful experiments were scored and split longitudinally, producing
392 shards of the tube with crystals adhered to the concave surface. Once opened, the crystal coatings
393 quickly darkened and turned yellow (Fig. 4). This change was attributed to water absorption
394 and/or oxidation, and further indicated that the glass tube had remained sealed during and after
395 the experiments. Unfortunately, this change complicated the analysis of the deposits because as
396 they hydrated, the adhesion of the gold coating for SEM observations was impaired, and
397 sometimes caused the deposits to slough off the inner wall of the tubes. Furthermore, euhedral
398 vapor-deposited crystals commonly lost their morphology upon opening of the tubes and
399 deliquesced into residues lacking any discernable crystal form. In attempt to preserve the crystals
400 once the tubes were opened, they were stored in a vacuum desiccator until ready for SEM
401 analysis. Even with this precaution, the loss of crystal form impeded the use of SEM imaging to
402 identify some crystals through the characteristic morphological forms of their crystal system.

403 **4.1 Source material**

404 The spent source material consisted of both crystals and glass, irrespective of use of glass
405 or powdered reagent mixture as the initial source. Although the temperature at the hotspot likely
406 remained above the liquidus temperature of the volatile-bearing initial sources, crystalline phases
407 formed from the silicate melts during degassing. Some of the crystals in the spent sources may
408 reflect quench crystals arising from our inability to rapidly drop the temperature of such large
409 experimental charges below the solidus (since the evacuated tube acts like a vacuum bottle).
410 However, some degree of isothermal crystallization is also expected simply due to loss of
411 dissolved volatiles, specifically Cl from the melt, and hence solidus temperature rise (e.g.,
412 Filiberto et al., 2009). The spent source material was highly vesiculated, clearly indicating that
413 boiling (vapor loss) had occurred and that we had indeed attained a high ratio of gas to silicate
414 melt. The fine-grained, broadly-disseminated crystals in the spent source made reliable EMPA
415 analysis of the bulk composition of the spent source difficult.

416 Thermogravimetric analyses (TGA) of I(Cl+S) glass source material was carried out
417 using a Netzsch STA 449C Jupiter Thermo-microbalance, in an N₂ gas stream as temperature
418 was ramped up slowly (10 degrees/minute) to 1150°C. These measurements demonstrated that
419 the source magma lost 8.3% of its weight during degassing. In addition, careful weighing of
420 capsules loaded with I(Cl+S) reagent mix before and after degassing were made on a limited
421 number of experiments where the capsule had not strongly adhered to the silica glass tube. These
422 measurements are within 1 wt% of the TGA results the glass source.

423 **4.2 Vapor-deposited phases**

424 **4.2.1 Mineralogy**

425 The crystals lining the upper portion of the tubes were small and strongly adhered to the
426 inner walls, thus, making it difficult to mechanically remove them. Therefore, tubes were split
427 open and broken. Glass shards were coated in gold for scanning electron microscopy (SEM) and
428 energy dispersive spectroscopy (EDS) analysis to determine the morphology and chemistry of
429 each mineral phase or coating present. These analyses were carried out using a LEO Gemini
430 1550 SEM/EDS at the Department of Materials Science at Stony Brook University. The identity
431 of most vapor-deposited minerals was inferred from these observations.

432 The crystal habit of grains that retained their form (as revealed by SEM), proved a useful
433 phase indicator when combined with qualitative EDS analysis. Figures 5 and 6 show these forms
434 and EDS spectra for both I(Cl+S) and I(Cl+HiS) sources. Halite was readily identified by both
435 its chemistry and cubic habit. Sylvite is the inferred K- and Cl- bearing phase observed, based on
436 EDS analyses as well as the likelihood that sylvite would be associated with halite. Iron oxides
437 crystallized from the vapor (experiments A-35, -37, and -39 in Table 2) from both source
438 compositions. They commonly formed octahedra, indicating a cubic crystal system and
439 suggestive of magnetite or maghemite. Iron chloride was found in all Cl-bearing experiments,
440 identified using EDS only as it lacked a well-defined crystal form. In experiments using the
441 I(Cl+HiS) source, pyrrhotite (or troilite) was identified through EDS and hexagonal/monoclinic
442 morphology. Pyrite was tentatively identified at the lowest temperatures of the (Cl+HiS) source
443 experiments due to its cubic shape and higher S/Fe ratio. In addition, a significant amount of
444 native sulfur was deposited as bright yellow spherical blebs in the uppermost (coolest) location
445 of the tube. A minor amount of native S was also seen at the cool end of the tube for the I(Cl+S)
446 source. EDS indicated the presence of an unknown silica phase in several experiments in small
447 rounded clusters in the I(Cl+S) source experiments; importantly, these were not found in the

448 silica glass tube after the S- and Cl-free experiment and therefore, were not simply related to the
449 silica glass tube.

450 The identity of the Fe-oxide could not be determined by SEM. For this reason individual
451 grains from the lower temperature region of the I(Cl+S) deposits (where the oxide octahedra
452 were large and could be easily isolated, Fig 5) were removed from the glass shards, placed in
453 paraben oil to prevent oxidation or hydration, and taken to the Advanced Photon Source (APS)
454 of Argonne National Lab for Synchrotron X-Ray Diffraction (SXRD) analysis. Single crystal
455 XRD yielded unit cell parameters that most closely matched the maghemite (γ - hematite
456 ($a=8.337(7)$ Å, $b=8.337(7)$ Å, $c= 8.337(7)$ Å, $\alpha=\beta=\gamma=90^\circ$) and hematite α - ($a=b=5.0278(5)$ Å, $c=$
457 13.7368(15) Å, $\alpha=\beta=90^\circ$, $\gamma=120^\circ$) structures. The maghemite may have formed from oxidation
458 of original magnetite during cooling of the tube (e.g., Jubb & Allen, 2010; Salazar et al., 2011).
459 Its unit cell dimensions here indicate no titanium in the solid solution, that is, essentially end-
460 member γ - Fe_2O_3 , (with no magnetite component). If it formed from oxidation of magnetite, then
461 the magnetite also was the pure Fe endmember. This would suggest that Ti is not transported to
462 any significant extent by the vapor.

463 The iron chlorides found were suggestive of molysite (ferric chloride) due to the highly
464 deliquescent nature of this material and the formation of a yellow-colored liquid (brine) when
465 exposed to moisture in the air (Fig. 4). To verify this identification, confocal Raman
466 spectroscopy was performed at the Vibrational Spectroscopy Lab at Stony Brook University on
467 the high iron + chlorine coatings in sample A-9 and the spectrum compared to an analysis of
468 dehydrated commercial-grade ferric chloride, FeCl_3 . Analysis of both was carried out using a
469 green laser with a wavelength of 514 nm. Figure 7 shows that similar features exist in both
470 spectra at Raman shifts of 400, 500, and 670 cm^{-1} , supporting the conclusion that the iron

471 chloride is molysite. The strong peak in the vapor-deposited material at ~ 200 cm⁻¹ is a second
472 phase co-existing with the molysite. Potential candidates of the second phase are sylvite and
473 sulfur (for the high S composition), as these phases have peaks within the observed Raman shift
474 range and both of these phases were already identified in this sample. However, the greenish
475 color of the chloride that adhered the maghemite to the glass tube prior to opening of the tube
476 and exposure to air hints that the primary iron chloride precipitated by the gas may have actually
477 been laurencite (FeCl₂) and that the molysite was secondary to oxidation of laurencite.

478 Coatings on these minerals were also noted. These may have formed during cooling after
479 removal of the tube from the furnace. Alternatively, particularly because the droplet-like
480 appearance of the regions in which they occur, some may have formed during dehydration of
481 brine (formed either during cooling of the tube or when the deliquescent salts were exposed to air
482 after opening the tubes) upon exposure to the SEM vacuum. As seen in both Figures 5 and 6,
483 there is permissive evidence that the iron oxychloride formed in this way.

484 Table 2 summarizes the vapor-deposited phases positively identified for each experiment.
485 As only two source compositions were used, additional experiments tested the replicability of the
486 technique. Importantly, due to the large areal extent of the interior of the long tubes and the small
487 SEM footprint, only the presence of a phase directly analyzed by SEM is definitive, as absence
488 may simply be a result of a phase being overlooked due to grain size or distribution within the
489 tube. Experiments A-35, A-36, and A-37 exemplify this. They show that the vapor-deposited
490 assemblage should include maghemite and silica even though analysis of two of the three tubes
491 showed only one of these two phases. Because of the strong possibility that a phase could be
492 overlooked in the tube, the identification of a new phase in replicate experiments, but for longer
493 duration of the degassing, does not mean that the phase was not present after the shorter duration

494 degassing. This may be exemplified by the presence of silica in the assemblage of experiment A-
495 13, but not in A-9; it may simply have been overlooked in A-9 perhaps because of smaller cluster
496 size. The apparent lack of hematite in the long duration experiment A-30 using a powder source,
497 but its identification in the shorter duration run using glass source (A-39) may similarly be
498 caused by oversight. Within the small temperature difference investigated here using the glass
499 source no temperature-induced difference in vapor-deposited assemblages was noted.

500 **4.2.2 Composition of bulk vapor-deposited material**

501 For experiments A-21, A-24, and A-40 of Table 2 using the I(Cl+S) source, the identities
502 and relative abundances of cations within the upper part of the tube that contained most of the
503 vapor-deposited material were determined by inductively coupled plasma optical emission
504 spectrometry (ICP-OES) analysis. After each of these experiments, the upper portion of the tube
505 containing the visible deposits was first weighed, then then fully submerged in a 3M nitric acid
506 solution and left to soak at room temperature for several days. After all visible solids were
507 dissolved from the interior of the tubes, the tubes were removed from the solution, dried, and
508 reweighed. The mass of total dissolved vapor-deposited solids in each partial tube was obtained
509 by the weight of the tube before and after dissolution. The total concentration (by weight) of the
510 dissolved deposits in the acid solution is the weight of total dissolved solids/weight of acid and is
511 listed in Table 3 as Total Solid Concentration. Importantly, if hydration (or oxidation) of any
512 mineral phase (e.g., hydration of molysite to $\text{FeCl}_3 \cdot 6\text{H}_2\text{O}$) took place prior to weighing of the
513 glass tube (before acid dissolution), the weight of total dissolved solids would be artificially
514 elevated. Therefore, the partial tubes were weighed as soon as they were removed from the
515 drying oven.

516 The nitric acid solutions containing dissolved vapor-deposited material were analyzed by
517 ICP-OES for all of the cations present in the source material (Table 1), however only Na, K, and
518 Fe had concentrations above 1 ppm. Note, this analysis did not include Si because it would not
519 be possible to distinguish Si dissolved from the silica glass tubes from dissolved vapor-deposited
520 Si. Table 3 summarizes compositional data for the solute from the dissolution. Iron is the most
521 abundant cation in the deposits with lesser amounts of Na and K. The concentration of each of
522 the other cations analyzed is less than 1 ppm, with many on the order of tens of ppb, consistent
523 with their absence in the mineral phases identified by SEM. Mass balance for the cations listed in
524 Table 3 based on the total solids concentration can be met by a combination of primary halite,
525 sylvite, molysite, Fe_2O_3 , and secondary ferric chloride hexahydrate. However, because of non-
526 uniqueness, the relative abundance of each of the Fe-bearing minerals is uncertain. The
527 differences between the analysis of A-21 and A-24 indicate the relative uncertainty, as the same
528 source I(Cl+S) mix was used. The difference in total concentration of solids for the glass source
529 rather than the mix is most likely due to the lower amount of glass source used in experiment A-
530 40 compared to the amount of mix in experiments A-21 and A-24.

531 The ICP- OES results indicate that alkali complexes preferentially degassed relative to Fe
532 complexes as suggested by the lower Fe/total alkalis (molar) ratio in the vapor deposits (Table 3)
533 relative to that of the starting material (e.g., 3.1-3.5). This reduction in Fe/total alkalis (molar)
534 was greater for the glass source than the mix source suggesting that Fe may have been more
535 tightly bound in the glass source. Perhaps with longer experimental run times, however, these
536 different source structural states would have yielded the same bulk cation of the vapor-deposited
537 material. Nonetheless, both source types produced the same vapor-deposited mineralogy. This

538 suggests that variations in the degassing path for Cl and S-bearing magmas may produce similar
539 vapor-deposited minerals.

540 **4.3 Oxygen Fugacity**

541 The oxygen monitor assemblages were recovered at the same time the tubes were opened.
542 XRD analysis of the monitor in the Cl- and S-free experiment (Experiment A-22 I(NVA) at 1150
543 °C) coupled with the calibration of the 2Θ with oxide composition of Lindsley (1976), showed a
544 slight shift to a more oxidized compositional pair (Table 4; Fig. 8) from Usp₄₈Mt₅₂ and Il₇₂Hm₂₈
545 to Usp₄₄Mt₅₆ and Il₇₀Hm₃₀ and an increase in Hm solid solution abundance relative to spinel (as
546 seen by the intersection of the tieline and “redox” line in Fig. 8), consistent with oxidation. This
547 small change in composition of the oxide pair yields a change in oxygen fugacity within the
548 uncertainty of QUILLF calculations and indicative of NNO+0.6(±0.1) log units. The fact that the x-
549 ray pattern showed a clear, albeit small, change from the original monitor suggests that the
550 monitor acted as a redox probe, not as a buffer, and that the redox state of the source was higher
551 than NNO. If the oxides attained equilibrium within the run duration, then the oxygen fugacity is
552 constrained to have been NNO+0.6. Based on the experimental durations of Webster & Bright
553 (1961) for oxides far from equilibrium, it is likely that the oxide pair in our experiments had
554 sufficient time to equilibrate. Since water was the only major dissolved volatile, the absence of a
555 major shift in composition of the monitor verified that loss of water alone by degassing did not
556 affect the redox state at the hotspot (Waters & Lange, 2016).

557 Based on the XRD spectrum of the monitor in the A-21 experiment (which used the
558 I(Cl+S) source), the oxides showed significantly more oxidation than that in the Cl- and S-free
559 composition, shifting from the assemblage Usp₄₈Mt₅₂ and Il₇₂Hm₂₈ to Usp₂₉Mt₅₆ and Il₆₀Hm₄₀

560 after the degassing. When computed through QUIIF these oxide compositions however, do not
561 represent an equilibrium pair at the temperature of the source; instead, they indicate a
562 temperature of over 150 °C lower than the actual temperature. If the Ilm_{ss} composition is correct,
563 the co-existing Usp_{ss} should have been $\text{Usp}_{40}\text{Mt}_{60}$ (Fig. 8). This would suggest that the ulvöspinel
564 solid solution was preferentially oxidized relative to the ilmenite solid solution upon exposure to
565 the magmatic gas. If the Ilm_{ss} composition is incorrect, the computed Ilm_{ss} ($\text{Ilm}_{48}\text{Hm}_{52}$) would
566 not preserve the bulk Fe/Ti ratio of the initial monitor and would suggest that Fe was transported
567 to the oxides by the gas. Either situation suggests that the gas may react with the oxides, making
568 a two-oxide monitor unreliable at best, and this interaction has the potential to change the gas
569 chemistry. Therefore, additional experiments were not run with an oxygen monitor.

570 **5 Discussion**

571 The results of the degassing experiments of the Cl- and S- bearing source compared with
572 the Cl- and S-free source underscore the importance of Cl and S in magmas for the formation of
573 vapor-deposited phases. The experimental setup yielded sufficient quantity of deposited material
574 for analysis; furthermore, the analysis showed that reproducible results were readily obtained.
575 The experiments produced deposits generally consistent with the vapor-deposited minerals
576 collected at the Erta Ale vent (e.g., Zelenski et al., 2013). However, just as for terrestrial
577 fumarolic gas sampling in glass tubes, correlating a precise temperature with a specific
578 assemblage is not straightforward because of the superposition of cooler phases during cooling
579 of the tubes. The temperature regions mentioned below strictly reflect the original temperatures
580 of the experiment before removal and cooling of the tube.

581 In the experiments with the I(Cl+S) source (Fig. 5), Fe/Na/K chlorides are found
582 throughout the temperature region ~800-300 °C, with evidence of silica deposits in this region as
583 well. Within the temperature regime 500-300°C, abundant maghemite appears as individual
584 grains embedded in a matrix of chlorides (molsite+halite+sylvite). It is possible that the
585 maghemite was originally magnetite before conversion during cooling and oxidation. Below
586 300°C, few deposits are visible other than a ring of orange material on the glass that may have
587 been hydrated ferric chloride (perhaps ferric chloride hexahydrate). Native sulfur is found at the
588 coolest end of the tube. All phases within the region of 700-500°C appeared to have secondary
589 coatings that may have been produced during cooling of the tubes, by reaction among vapor
590 deposited minerals, or by gas/mineral interaction, with iron oxychloride as the most significant
591 example. Hematite was noted with maghemite during analysis of a single octahedron; this may
592 have formed by oxidation upon cooling of the tube after the experiments.

593 For the sulfur-rich source (Fig. 6), iron oxides are visibly precipitated with chlorides at
594 ~700°C, along with silica deposits. At ~500°C is a region with the assemblage sylvite+halite+
595 molsite+pyrrhotite+maghemite. Below about 400°C iron oxides are no longer observed.
596 Sulfides, specifically pyrite, persist to as low as 300°C, at which point chlorides are no longer
597 found. At the lowest temperatures, <100 °C, native sulfur “droplets” are adhered to the top of the
598 tube.

599 The experiments do not provide direct access to the gaseous species during the
600 experiments, but some inferences can be made based on the assemblages. With 0.4 wt.% water in
601 the starting glass, there was undoubtedly some H-bearing gaseous species present in the vapor
602 phase. S-species in the vapor would be dominantly SO₂ at the pressure of the experiments (~1
603 bar), with significant S₂ and minor H₂S (Gaillard & Scaillet, 2009). Some of the Cl was likely

604 transported as HCl. However, as it is generally accepted that the vapor species of salts and oxides
605 in high temperature gases are associated units (Krauskopf, 1964; Renngli et al., 2017), additional
606 metal chloride gaseous species were likely also present. Although we cannot definitively
607 correlate the deposited minerals with an equivalent charge-neutral associated vapor species
608 (Renngli et al., 2017), the fast, high-temperature deposition in the silica glass tube may permit a
609 simple process of sublimation (Yudovskaya et al., 2008). In this case, the Fe content of the net
610 composition of the vapor-deposited material would be primarily due to the transport of Fe as iron
611 chloride gaseous species, as concluded by Renngli et al. (2017), although Fe-oxide, and Fe
612 sulfide species may also exist. The high Fe content of the net vapor deposit composition is likely
613 correlated to the high Cl content of the melt, as Fe-chloride complexes can partition even more
614 strongly than NaCl and KCl into exsolved fluid, liquid, or gas (Pokrovski et al., 2013).

615 **5.1 Redox conditions of the vapor deposited phases.**

616 Assessing the distribution of oxygen in the tube is important as oxygen plays a central role in
617 dictating the redox state of the gaseous species. It is commonly assumed that in experiments
618 utilizing short evacuated silica glass ampoules (i.e., in a small temperature gradient), that the
619 oxygen fugacity throughout the tube in “nominally volatile-free” systems equals the sample at
620 the hotspot, even without an additional oxygen buffer. This conclusion still holds for long
621 evacuated tubes in a strong thermal gradient as long as O₂ is the only species. This can be seen
622 by the generalized expression for diffusion of a chemical species in the absence of external
623 forces over a thermal gradient:

624
$$\mathbf{J}_i = -D_i C \mathbf{d}_i - D_i^{(T)} / M_i \nabla \ln T \text{ where } CRT \mathbf{d}_i = C_i \nabla T, p \mu_i + (C_i V_i - \omega_i) \nabla P, \quad r4$$

625 (Equation 14.6-1 of Deen, 2013) where \mathbf{J}_i is the diffusive flux of chemical species i , D_i is the
626 diffusion coefficient of species i , C is the overall concentration of the phase at a point in space,
627 M_i is the molar mass of species i , ω_i is the volume fraction of species i in the phase. V_i is the
628 partial molar volume of species i . ∇P is the pressure gradient between two specified points, and T
629 is the temperature. μ_i is the chemical potential of gaseous species i and R is the universal gas
630 constant. $\nabla_{T, P}\mu_i$ is the isothermal, isobaric gradient in chemical potential, i.e. the change in
631 chemical potential purely due to differences in mixing entropy.

632 If oxygen is the only gaseous species, the Soret Thermal Diffusion coefficient, $D_i^{(T)}$, is
633 zero since the Soret effect/thermal gradient-driven diffusion is not observed in pure phases
634 (Platten, 2006). Additionally, the $(C_i V_i - \omega_i) \nabla P$ term is zero in a pure gas, since the molar volume
635 is the inverse of the concentration of the phase and ω_i is 1. Therefore, even in a temperature
636 gradient, the diffusion of species i reduces to the Teorell equation (Gorban et al., 2011):

637
$$\mathbf{J}_i = -u_i \nabla_{T, P} \mu_i$$

638 where u_i is the mobility of species i . At steady state in the tube, in the absence of a reaction and
639 with no convective motion:

640
$$\mathbf{J}_i = 0 = -u_i \nabla_{T, P} \mu_i$$

641 where u_i is approximately constant. Because of this, oxygen in the silica glass tube will diffuse
642 until the chemical potential of oxygen is the same throughout the tube (that is, the chemical
643 potential gradient must be zero) along the thermal gradient. As long as the fugacity coefficient is
644 approximately 1 (a very reasonable assumption for a dilute pure gas phase at moderate
645 temperature), oxygen must diffuse throughout the entire tube until the pressure is equalized at all

646 points regardless of temperature. Combined with the boundary condition that the fugacity of
647 oxygen at the position of the source is that of ~NNO at 1150°C at steady state, diffusion will
648 occur until the fugacity of oxygen throughout the entire tube is that of the source at the hotspot.
649 The requirement that the oxygen fugacity be the same throughout the tube in this case precludes
650 a change in oxygen fugacity along an oxygen buffer curve in the cooler portion of the tube, even
651 if an oxygen buffer were present at the hotspot. Because of the stronger oxidizing effect of a
652 given oxygen fugacity at lower temperatures, constant oxygen fugacity would produce
653 assemblages that were more oxidized at higher levels in the tube. The condition of constant
654 oxygen fugacity throughout the tube is not retained however, in a multicomponent gaseous
655 mixture where O₂ is a minor constituent. But it can be considered as providing the upper limit of
656 oxygen fugacity in the system.

657 For a multi-component vapor, the two components of the overall diffusion equation
658 which we set to zero - one for thermal-driven diffusion and one for molar volume differences-
659 driven diffusion - would be nonzero. If the quantity of other gases were small compared to the
660 quantity of O₂, we could neglect the thermal driven diffusion, and as a result, no pressure
661 gradient would form, and we would recover our original result. But for the multicomponent
662 gases produced in these experiments, thermal diffusion (known as the Soret effect in liquids)
663 becomes an important player. This is a well-recognized phenomenon which causes concentration
664 gradients to develop in an originally homogeneous gas mixture placed in a strong temperature
665 gradient (e.g., Bogatyrev et al., 2014; Chapman & Cowling, 1953; Chapman & Dootson, 1917;
666 Gillespie, 1939). This compositional gradient can exist in steady state due to a balance between
667 ordinary diffusion (which tends towards homogenization) and thermal diffusion (which induces a
668 separation of species, e.g., Deen, 2013). While no pressure gradient would develop in the tube,

669 the species with larger mass will be preferentially concentrated at the cold end (e.g., Chapman &
670 Dootson, 1917; Deen, 2013). Therefore, the concentration of oxygen is predicted to be lower at
671 the cold end of the tube relative to the concentrations of gaseous species such as SO_2 and neutral
672 salt complexes such as $\text{FeCl}_{3(g)}$.

673 Since thermal diffusion coefficients are difficult to obtain due to their temperature and
674 compositional dependence, assigning numerical values to the oxygen gradient in the tube is not
675 possible, yet the assemblages observed may produce some qualitative indication of oxygen
676 fugacity distribution in the tube. The oxygen fugacity set at the hotspot based on the results of
677 the I(NVA) oxygen monitor experiment was $\text{NNO}+0.6\pm0.1$. Figure 9 provides a reconstruction
678 of the oxygen fugacity along the tube based on observed phase assemblages and the assumptions
679 that (i) the sulfides and oxides are primary vapor-deposited minerals and their position in the
680 tube reflects the thermal gradient in the experiments, (2) maghemite formed by oxidation of
681 magnetite, so its presence indicates magnetite as the vapor-deposited phase, (3) the hematite
682 associated with maghemite in I (Cl+S) is secondary, that is, it formed during cooling after
683 removal of the tube from the furnace, and (4) the regions of the tubes removed for analysis
684 adequately reflect the temperatures regime noted. As shown in Figure 9, for both sources, the
685 presence of magnetite restricts the oxygen fugacity to the region between the HM and WM
686 buffer curves over much of the temperature space. Thus, there is a definite decrease in oxygen
687 fugacity with dropping temperature. Because no buffer was present in these experiments, the
688 lower fO_2 at lower temperatures in the tube is likely due to the thermodiffusion of gaseous
689 species discussed above.

690 **5.2 Implications for Martian fines.**

691 Magmatic vapor escaping from gas bubble-charged shallow magmas may have
692 contributed a significant amount of Fe, S, and Cl to the martian surface through vapor-deposition
693 of minerals during the late stages of martian magmatism when the gas ascending from a deep
694 plumbing system was OH-poor and S- and Cl-rich. Such deposits would not have been restricted
695 to large gas vents but could have been distributed across the surface of lava flows during passive
696 gas loss. This process would not transport significant amounts of Ca, Al, or Mg from the magma
697 and hence, would preclude the direct deposition of Ca- or Mg sulfates. Although direct vapor
698 deposition of Ca- and Mg-sulfates seems unlikely based on these experiments, such sulfates
699 could form during acid alteration of the surface via gas/rock interaction (e.g., Chouinard et al.,
700 2005; King et al., 2018; Stoffregen, 1987).

701 Passive degassing of a bubble-charged lava flow involves strong thermal gradients above
702 the lava surface and a change in the thermal profile with time as cooling of the surface of the
703 flow occurs. In this case, a clear spatial variation in type of vapor-deposited material would not
704 be expected. Instead there should be mixed regions of high and low temperature vapor-deposited
705 assemblages reflecting cooling of the gas above the flow. The mineral phases of the intermingled
706 assemblage could react with dropping temperature and form a set of secondary minerals that
707 obscure at least some of the primary assemblages, and these secondary minerals could have been
708 disproportionately represented in the martian fines. Such reaction could occur with no free
709 surface water. Changes in relative humidity as observed by MSL (Savijärvi et al., 2015) can lead
710 to deliquescence and subsequent efflorescence of some salts (e.g.,; Gough et al., 2014; 2016;
711 Nuding et al., 2014), potentially allowing deliquescent phases to incorporate other elements from
712 soluble salts as they become aqueous solutions and then re-solidify (Sklute et al., 2018).

713 Based on the experiments here, several changes likely occurred during cooling. The
714 absence of magnetite but plentiful octahedra of the metastable phase maghemite suggests
715 conversion of magnetite to maghemite as a consequence of the formation of a more oxidized
716 assemblage with dropping temperature. The possibility of maghemite being present at the surface
717 of Mars is evidenced by analysis of magnetic dust in situ (Bertelsen et al., 2004). Since the
718 magnetic properties of martian dust and soil are presumed to be dictated, as on Earth, by
719 magnetite and maghemite (Banin et al., 1993; Madsen et al., 1999; Morris et al., 2000; 2001), the
720 production of maghemite by vapor deposition on the surface of cooling lava flows provides an
721 important alternative production mechanism to that of the thermal conversion of lepidocrocite
722 via meteoritic impact (Banin et al., 1993; Morris et al., 1998) or its formation as a transient phase
723 in the transformation of ferrihydrite to hematite in the presence of phosphate or other ligands
724 capable of ligand exchange with Fe-OH surface groups (Barron & Torrent, 2002; Cumplido et
725 al., 2000; Torrent & Barron, 2000).

726 The co-existence of molysite and hematite (and maghemite) in the vapor-deposited
727 assemblages allows for the formation of iron oxychloride (FeOCl) by the reaction $\text{FeCl}_3 + \text{Fe}_2\text{O}_3$
728 $\rightarrow 3\text{FeOCl}$ at $\sim 350^\circ\text{C}$ (Dai et al., 2003; Halbert et al., 1980; Yang et al., 2013). This phase may
729 be reflected in the EDS spectra of Figs 5 and 6, and present in the fine-grained coatings. Iron
730 oxychloride is a Fenton-like catalyst, which according to Yang et al. (2013), exhibits unusual
731 efficiency for yielding OH radical by H_2O_2 decomposition and exceptional performance in the
732 degradation of persistent organic compounds (e.g., from carbonaceous chondrite impactors or
733 other organic sources). This has important implications for Mars in that it suggests if iron
734 oxychloride produced in the cooling gas column above martian lava flows couples with a
735 photochemically produced atmospheric oxidant such as H_2O_2 (Atreya et al., 2006) it would

736 contribute to destruction of organics on the martian surface. In fact, a lower than expected
737 organic yield has been noted by Zent & McKay (1994) based on the Viking Biology
738 Experiments and Ming et al. (2014) in their discussion of the analysis of the mudstone at
739 Yellowknife Bay, Gale crater.

740 There are various routes to destruction of FeOCl that could inhibit its identification in
741 martian fines. Iron oxychloride readily picks up atmospheric moisture and can produce
742 akaganéite (FeO(OH,Cl)) (Argo, 1981), a phase seen in the mudstone at Yellowknife Bay, Gale
743 crater (e.g., Vaniman et al., 2014), or $\text{Fe(OH)}_2\text{Cl}$, even at temperatures below 100°C. Upon
744 heating, $\text{Fe(OH)}_2\text{Cl}$ can lose some HCl and revert to (FeO(OH,Cl)), or, if all HCl is lost, form β -
745 FeOOH (Kanungo & Mishra, 1997).

746 Under even more humid conditions, FeOCl (or molysite directly) may have formed ferric
747 chloride hexahydrate as the magmatic gas cooled below 220–250°C, which was then deposited
748 into the fines (Zhang et al., 2017). Dehydration of the ferric chloride hexahydrate during heating
749 and analysis would add have added to the reported water budget yielded by heating samples from
750 Rocknest fines and the mudstone of the Yellowknife Bay Formation. Importantly, any remaining
751 chlorides may have produced perchlorates by irradiation of the martian surface by either UV
752 (Schuttlefield et al., 2011; Carrier & Kounaves, 2015), cosmic rays (Wilson et al., 2016), or both.

753 The spatial association of halite, molysite, and pyrrhotite in the vapor-deposited material
754 (Fig. 10) suggests that in the presence of small amounts of water and upon oxidation of the
755 pyrrhotite, all of the ingredients for making fine-grained jarosite would be available. Dutrizac
756 (2008) noted that jarosite is readily precipitated upon dissolution of KCl (and NaCl) and
757 molysite, provided that an independent source of sulfate is available. His experiments at 140°C

758 indicated that low sulfate concentrations resulted in the precipitation of hematite-jarosite
759 mixtures; higher sulfate concentrations result in the formation of only potassium jarosite. This
760 jarosite formation could occur as the surface of the lava flows continued to cool below 200°C.
761 By this temperature, as seen in the I(Cl+HiS) experiments, pyrite rather than pyrrhotite would be
762 stable and oxidation of pyrite could be an important step in the formation of jarosite (Zolotov &
763 Shock, 2005). McCubbin et al. (2009), however, noted the presence of secondary jarosite and
764 hematite surrounding pyrrhotite in a melt inclusion in pyroxene from the Miller Range (MIL)
765 03346 meteorite, suggesting that the conversion of pyrrhotite to pyrite may not be a necessary
766 first step. Since liquid water is not necessary to form the jarosite according to the calculations of
767 Navrotsky et al. (2005), it is possible that the fugacity of water was sufficiently high in the
768 magmatic gases by this stage and enhanced by relative humidity of the martian atmosphere that
769 this process could have occurred in the absence of liquid water and the presence of the magmatic
770 gas. Furthermore, as concluded by Navrotsky et al. (2005), once jarosite formed it could remain
771 stable on the martian surface as a component in the dust and soil.

772 If abundant deliquescent phases such as molysite were added to the surface during
773 magma degassing, it is likely that transient liquid brines could have periodically formed that
774 would have incorporated much of the soluble material that was deposited by magmatic vapor. If
775 terrestrial analogs are good indicators of brines like these, they would be quite acidic (Benison &
776 LaClair, 2003). This is seemingly difficult to reconcile with the proposed abundance of
777 carbonate (2-5 wt.%) in martian fines (Bandfield et al., 2003). However, it must be noted that the
778 carbonates are most likely formed in aqueous processes that are independent from those involved
779 in mineral deposition from magmatic degassing. Thus, it is possible that mechanical mixing of

780 the evaporative products of the brine and carbonate could be incorporated into the global dust
781 layer.

782 **5.3 How much material could have been added to the Martian surface by this process?**

783 Recent martian volcanism identified at Elysium (Plescia et al., 1993; Vaucher et al.,
784 2009), Olympus Mons (Chadwick et al., 2015; Mangold et al., 2010) and other locales on the
785 surface (Hauber et al., 2011), could have given rise to vapor-deposited minerals similar to what
786 we obtained experimentally. An important question remains regarding how much material this
787 process could have contributed to the surface. Quantification of the amount of vapor-deposited
788 material formed from a cooling lava is not a straightforward process as it will depend upon the
789 gas/melt ratio and the composition of the gas. The gas/melt ratio may be much higher than that
790 expected from simple volatile solubility limits (e.g., Filiberto & Treiman, 2009, Gaillard &
791 Scaillet, 2009; Righter et al., 2010). Wallace (2001) showed that terrestrial volcanic systems
792 release on average 10 times more SO₂ than can be accounted for by the erupted volumes of lava,
793 and attributed this to formation of a vapor phase at depth and migration of this phase upward
794 through the magma plumbing system. As these bubbles of gas concentrate, they effectively enrich
795 the upper portions of the magma chamber with exsolved gas. With the higher abundance of Cl
796 and S and the lower amount of water in late martian magmas relative to terrestrial magmas
797 (Filiberto & Treiman, 2009; Filiberto et al., 2016a, b), the amount of sublimates arising from
798 passive degassing flows may be much higher than from terrestrial lava flows where water and
799 CO₂ remain the dominant gases given off.

800 When considering that martian magmas appear to inherit up to 0.3 wt.% Cl (Filiberto &
801 Treiman, 2009), and 0.4- 1.4 wt.% S (Gaillard & Scaillet, 2009; Righter et al., 2010) from their

802 source, the concentrations of these volatiles in our experiments did not produce an unreasonably
803 high gas/melt ratio. The experiments, therefore, can be used to provide an idea of the sublimate
804 load that could have been added to the surface by recent martian lava flows. Our estimation is
805 necessarily simplified and takes the weight of sublimes relative to the weight of glass source to
806 determine the relative amount of sublimes produced. The experiments show that between 1.9
807 wt% (for the I(Cl+S) composition) and 3.7 wt% (for the I(Cl+HiS) composition) of the mass of
808 the glass produced in the high-pressure synthesis was converted to the precipitates observed.
809 [The actual mass transported from the melt was higher than this since it would have included
810 vapor phase components that did not precipitate a solid phase, such as SO₂ and H₂O.]

811 Table 5 shows projected quantities of vapor-deposited minerals contributed to the surface
812 by recent igneous activity Mars. The calculations assume (i) that the vapor-deposited minerals
813 from a lava of Irvine composition is a reasonable analog for other martian magmas and the initial
814 volatile load at depth is similar to that of the experiments, (ii) that 2 wt% of the lava mass is
815 converted to vapor-deposited minerals as per the lower value of the experiments, (iii) that the
816 density of the lava is 3000 kg/m³ and that of the vapor-deposited material is 4000 kg/m³ (roughly
817 intermediate between chlorides, sulfides and oxides). The computed thickness of global coverage
818 by vapor deposits contributed by young volcanism (Table 5) is markedly similar to the
819 thicknesses predicted by Franz et al. (2018) (however, their computations assumed the formation
820 of vapor-deposited sulfate rather than the sulfides and chlorides observed here) with young
821 Olympus Mons eruptions alone producing enough vapor-deposited material to blanket the planet
822 to a thickness of 15 cm.

823 Although young volcanism is expected to have made a major contribution of Cl and S to
824 the present day dust though vapor deposited material, these contributions may be masked by

825 contributions from older fine-grained formations susceptible to aeolian weathering. This can
826 probably be best exemplified by the Medusae Fossae Formation (MFF). Although the recent
827 volcanism from Olympus Mons could have contributed just as much vapor-deposited material as
828 the MFF (Table 5), Ojha et al. (2018) noted that the MFF provides the best chemical match to
829 surface measurements of Martian dust. The MFF has been considered an easily erodible
830 pyroclastic deposit and it is possible that its high Cl and S is due to vapor-deposited material on
831 the surface of the ash. The absence of sulfates in this unit (Ojha et al., 2018), suggests that the
832 prime contribution of Cl and S is through the formation of vapor deposited sulfides, native sulfur
833 and chlorides rather than by interaction of the glass and gas to form sulfates.

834 **6 Conclusions**

835 Experiments conducted using a typical martian basalt have demonstrated that when a lava
836 enriched in gas bubbles carrying an OH-poor, S- and Cl rich gas cools on an oxidized surface,
837 the magmatic vapors will deposit primary halite, molysite, sylvite, magnetite/maghemite,
838 pyrrhotite, pyrite, and sulfur over a range of temperatures between approximately 700 and
839 200°C. These phases can oxidize or react in the cooling gas column to form a variety of
840 secondary phases including maghemite, hematite, iron oxychloride, and possibly jarosite,
841 akaganéite and perchlorates which could be incorporated into the martian dust and widely
842 distributed. The fine material on Mars's modern surface may show a disproportionately large
843 load of vapor-deposited phases produced by low OH magmas.

844

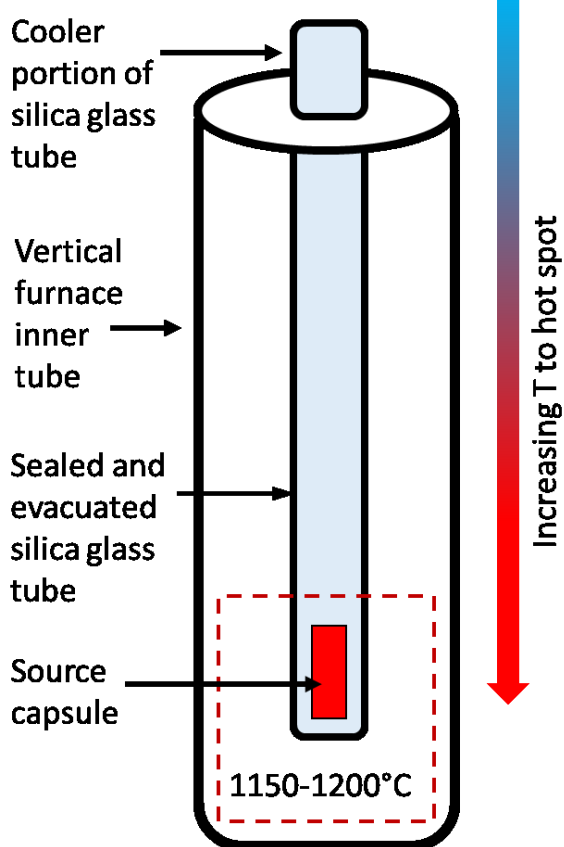


Figure 1. Schematic of experimental setup. The $\text{Au}_{80}\text{Pd}_{20}$ capsule containing the source material is placed in a long ($\approx 28\text{cm}$) evacuated and sealed silica glass tube within the vertical tube of a Pt-wound furnace (not shown). Note - Figure not to scale.

845

846

847

848

849

850

851

852

853

854

855

856

857

858

859

860

861

862



863

Figure 2: Silica glass tube containing I(Cl+S) glass source after cooling, with approximate temperatures of formation of primary vapor-deposited material indicated. Capsule containing the source is at bottom. Inset shows enlargements of the region in the tube containing well-formed octahedra adhered to the tube by a fine grained greenish yellow precipitate. Just below $\sim 300^{\circ}\text{C}$, a ring of orange fine-grained material was formed.

864

865

866

867

868

869

870

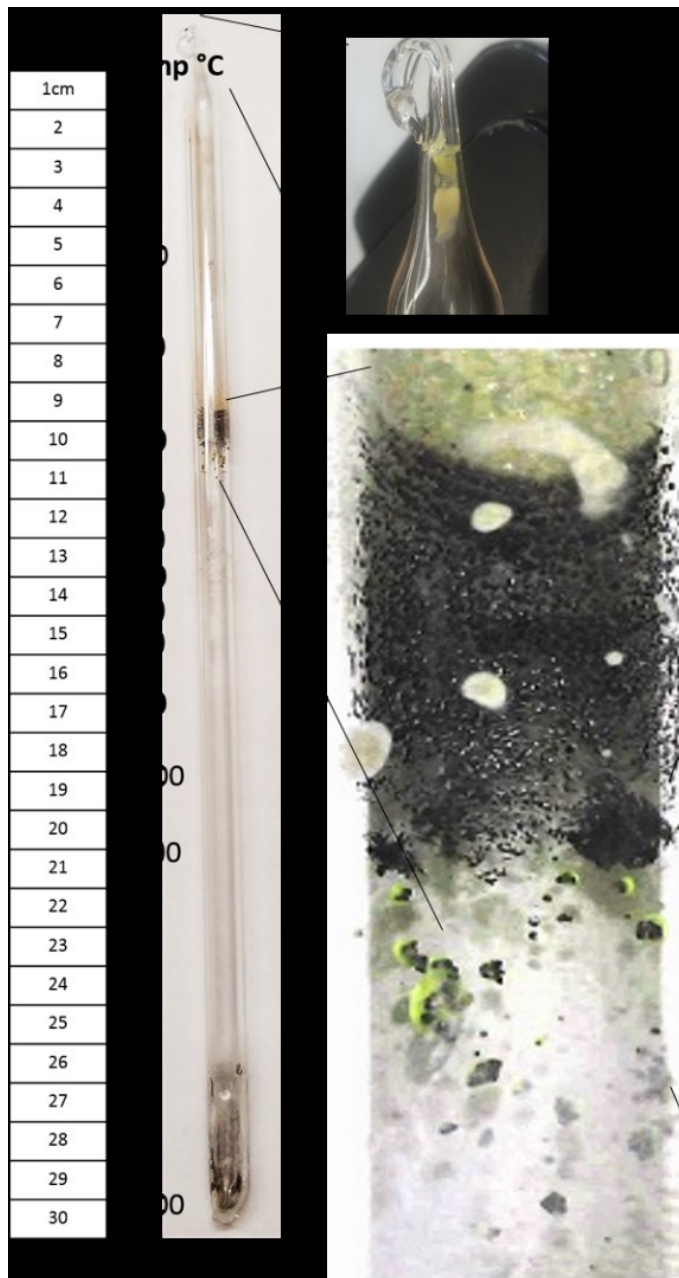
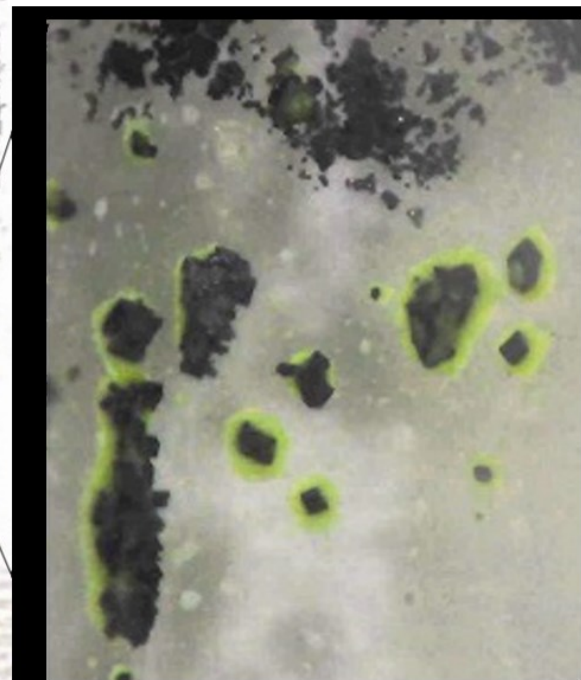


Figure 3: Silica glass tube containing I(Cl+HiS) glass source after cooling, with approximate temperatures of formation of primary vapor-deposited material indicated. Capsule containing the source is at bottom. Inset shows phases observed. Top, native S precipitate; the center and right show octahedra adhered to the glass wall by a greenish yellow precipitate below a region of massive deposition of finer grained dark material.





873

874 **Figure 4:** Silica glass tube containing I(Cl+HiS) glass source following degassing, before (a) and
875 after (b) opening.

876

877

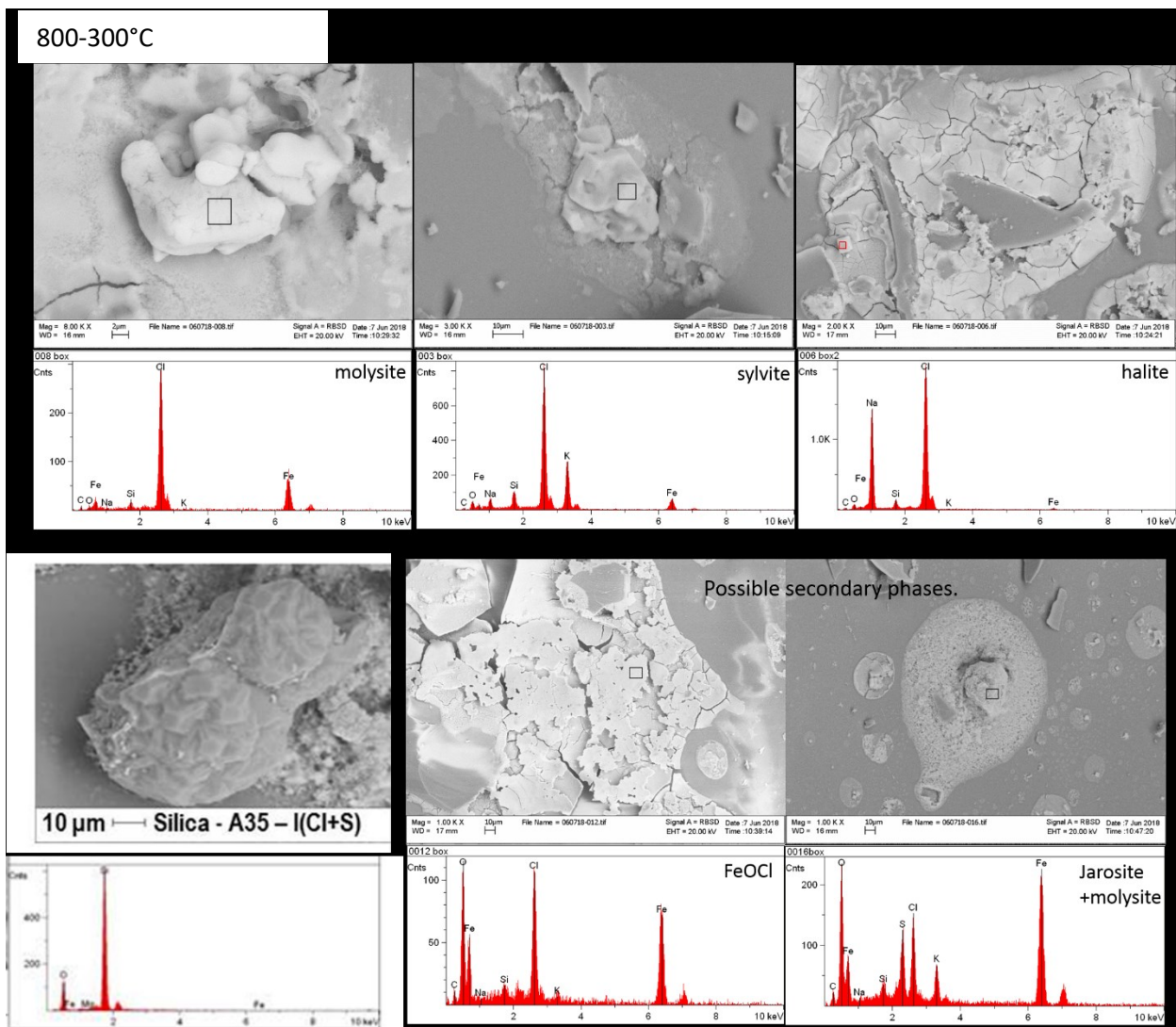
878

879

880

881

882 **Figure 5.** SEM images, EDS spectra, and inferred identity of vapor-deposited minerals in
 883 experiment A54 (I(Cl+S) source).

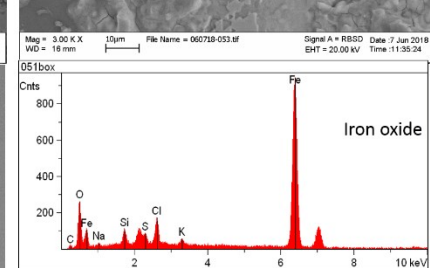
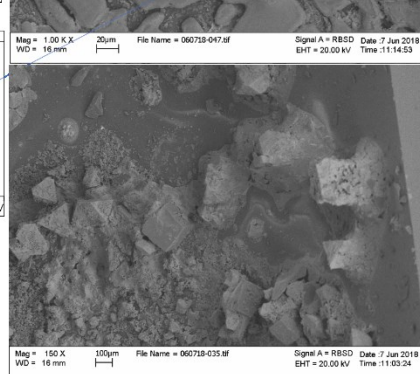
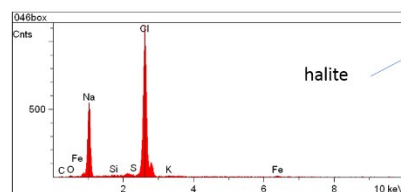
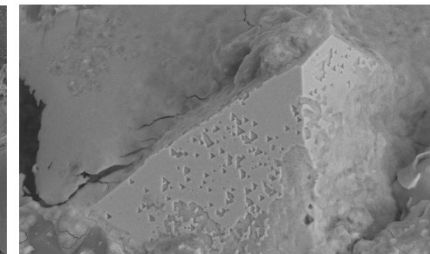
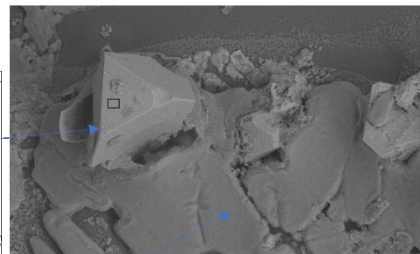
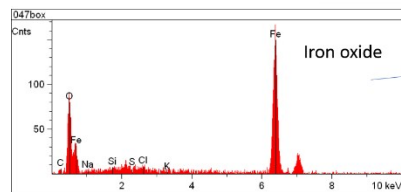


884

885

886

500-300°C



887

888

700-500 °C

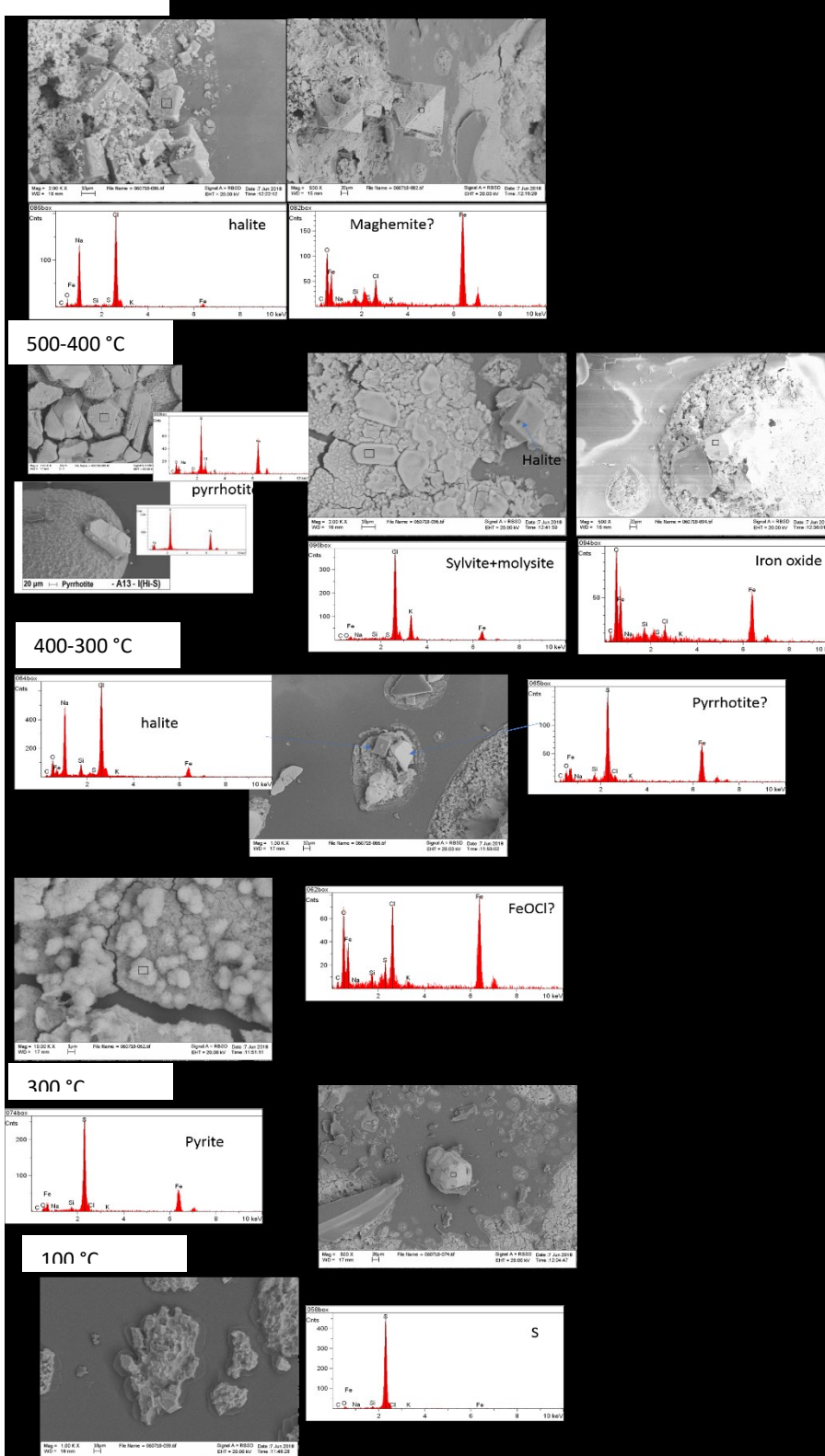
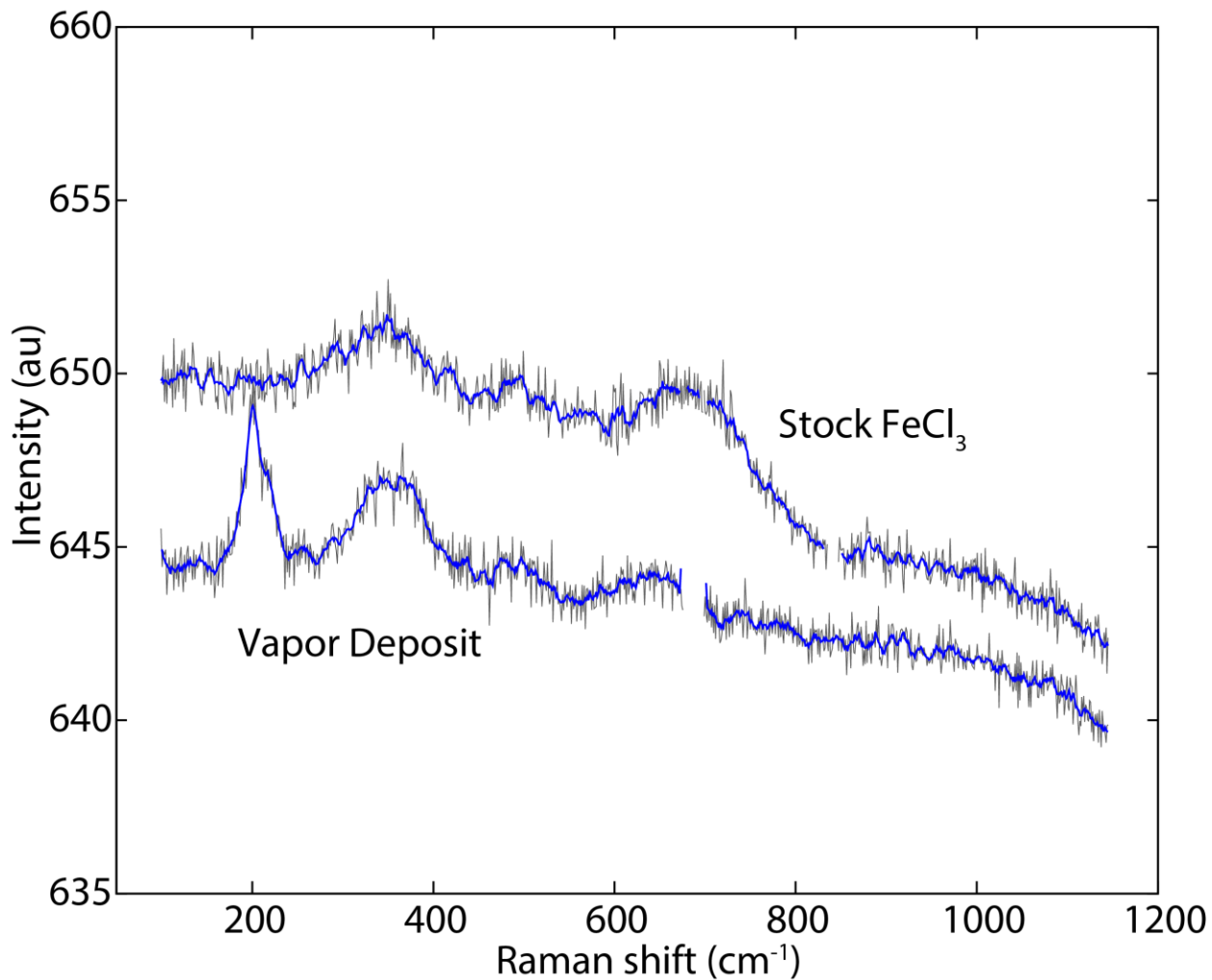


Figure 6. SEM images, EDS spectra and inferred vapor-deposited phases for experiments using the I(Cl+HiS) source.



891

892 **Figure 7:** Comparison of Raman spectra from dehydrated laboratory-grade ferric chloride and
893 vapor deposited material from experiment A-9 containing an iron-chlorine compound. Features
894 at 400, 500, and 670 indicate that the sublimate contains ferric chloride (molysite). Note: The
895 strong peak in the vapor deposit is a second phase, likely deposited at the same time as the
896 molysite. The gap in the spectrum at ~700 cm⁻¹ corresponds to a cosmic ray detected during the
897 analysis and deleted from the data. Intensity is shown in arbitrary units. Raw data are shown in
898 gray; blue lines represent data smoothed with a seven-channel boxcar filter.
899

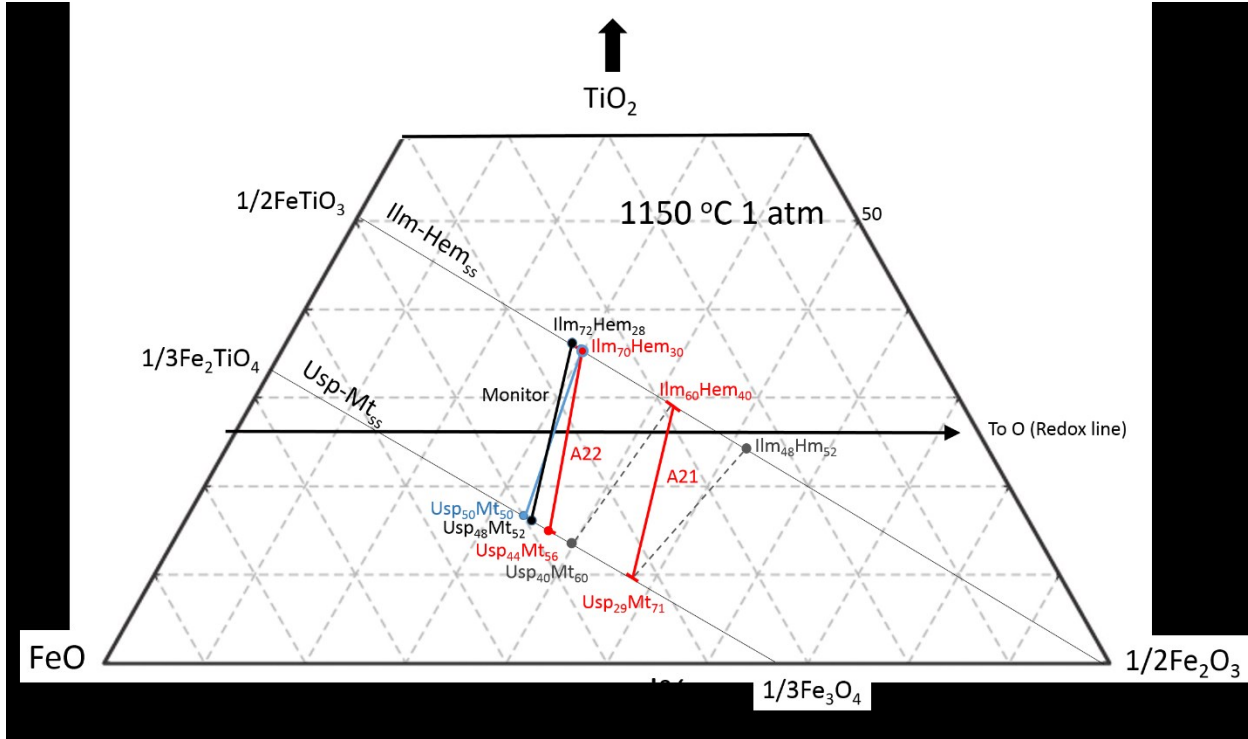
900

901

902

903

904 Figure 8.



905

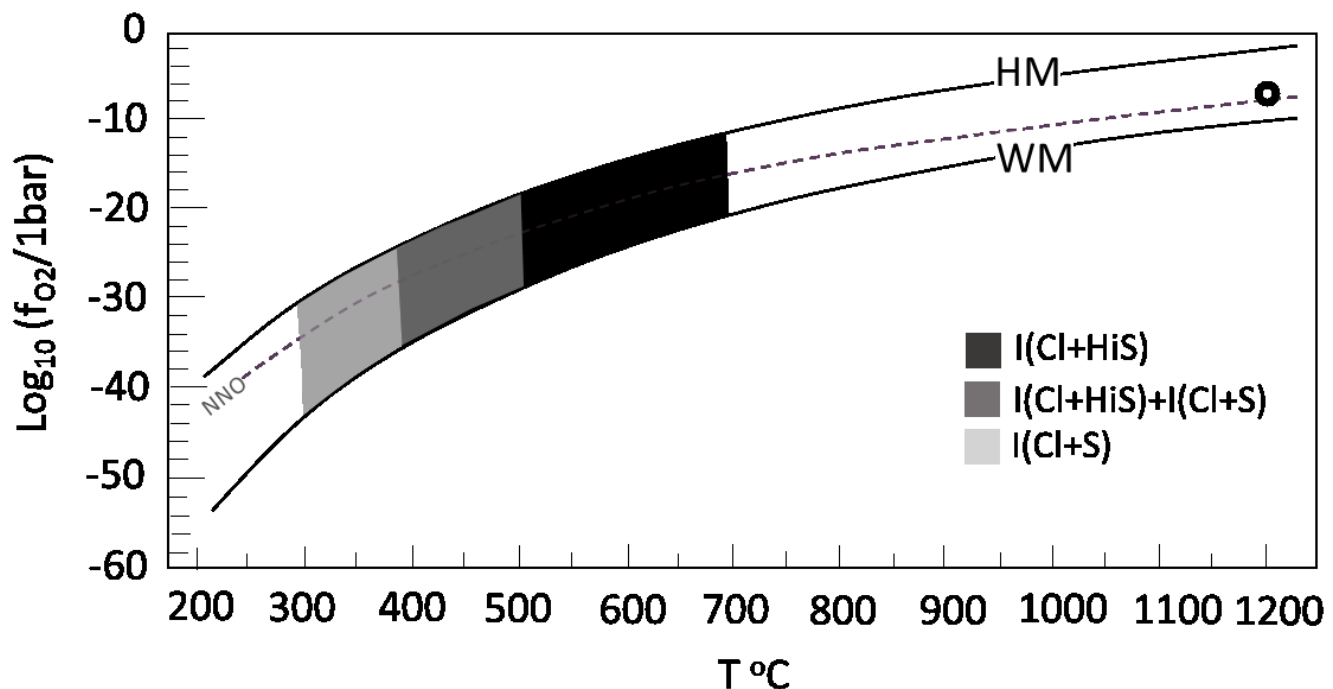
906 **Figure 8.** Compositions of co-existing Ilm-Hm_{ss} and Usp-Mgt_{ss} for the initial monitor and of the
 907 monitor after heating with the I(NVA) source (experiment A22) and the I(Cl+S) source
 908 (experiment A21). The endmembers of the solid blue line show the nominal composition of the
 909 initial monitor oxide before heating; the endmembers of the black line show the composition of
 910 the initial monitor oxides based on cell parameters and the variation of cell dimensions with
 911 changing composition of the solid solutions from powder XRD and the assignments of Lindsley
 912 (1976). The redox line shows the direction of oxidation for the Fe/Ti ratio of the oxide mixture.
 913 Note that the intersection of the black tieline with the redox line shows the 1:1 ratio of Ilm-Hm_{ss}
 914 and Usp-Mgt_{ss} loaded. The composition of the monitor after heating with the I(NVA) source
 915 (A22 red tieline) shows evidence for oxidation, not only in the shift of oxides composition but in
 916 the slight increase in modal abundance of IlmHm_{ss}. The monitor oxides after heating with the
 917 I(Cl+S) source (A21) showed major oxidation, and produced a disequilibrium pair. The dashed
 918 gray tielines indicate computed equilibrium pair using each oxide.

919

920

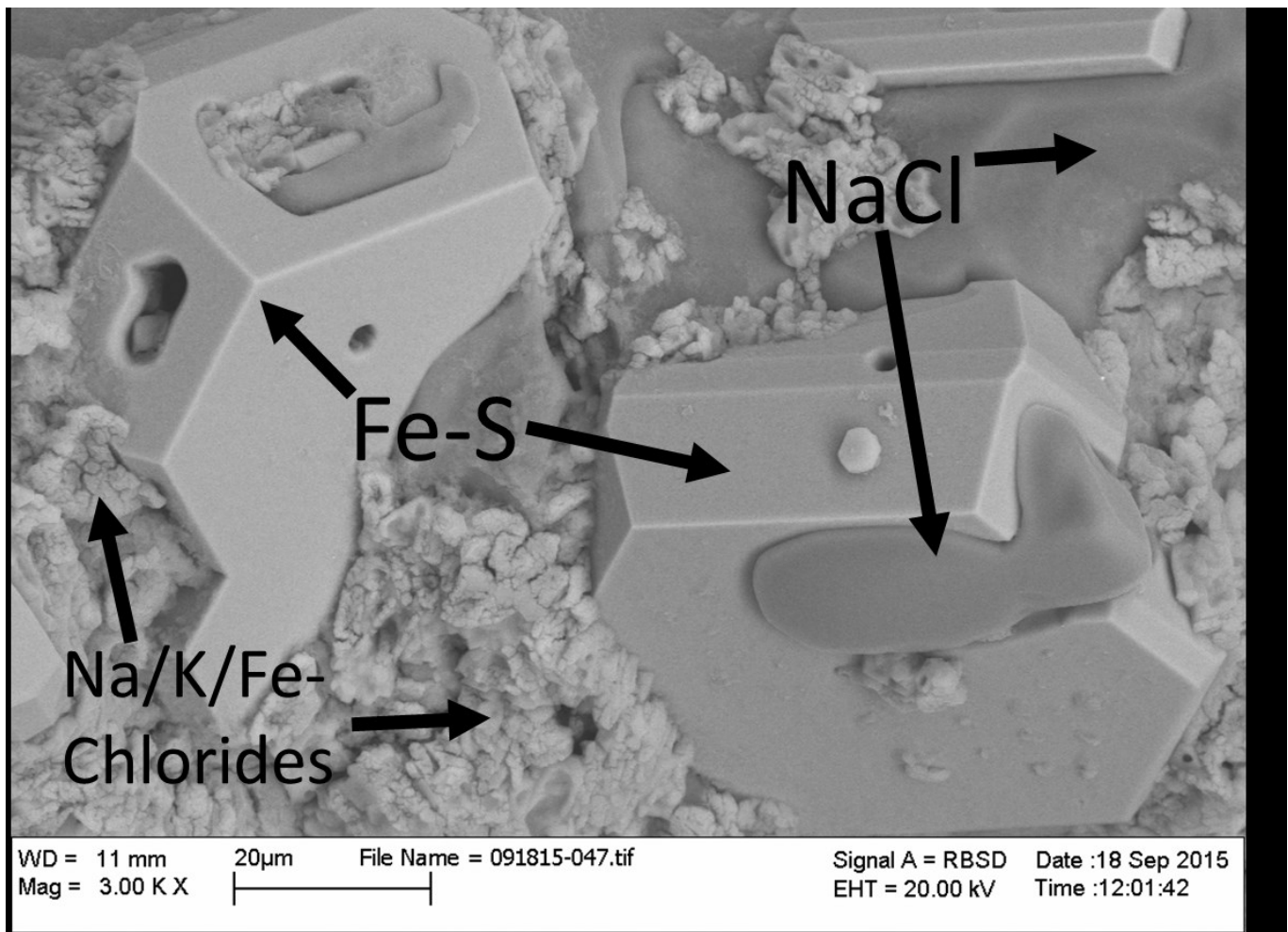
921

922



923

Figure 9. Constraints on the variation of the oxygen activity with temperature along the thermal gradient in the experimental silica glass tubes based on the presence of magnetite (assuming primary precipitation of magnetite before later conversion to maghemite). Open circle is initial source at 1200 °C. Legend indicates the sources used in each region. HM: hematite-magnetite buffer; WM: wustite-magnetite buffer; NNO: Nickel-Nickel oxide buffer as computed using the database Robie et al. (1979).



924

925

Figure 10: BSE image of coexisting phases for the I(Cl+HiS) source.

926

927

928

929

930

| Sample | Mars Bulk Crust ^a | Irvine Unbrushed ^b | Soil-Corrected Irvine ^b | Volatile - Free Irvine | I(NVA) ^c (11) ^d | 1 σ ^e | I(Cl+S) ^f (8) | 1 σ | I(Cl+HiS) ^g |
|------------------------------------|------------------------------|-------------------------------|------------------------------------|------------------------|---------------------------------------|-------------------------|--------------------------|-------------|------------------------|
| SiO₂ | 49.01 | 45.98 | 46.94 | 47.30 | 48.90 | 0.16 | 48.73 | 0.35 | 47.03 |
| TiO₂ | 0.95 | 1.04 | 1.06 | 1.07 | 1.13 | 0.01 | 1.00 | 0.04 | 1.05 |
| Al₂O₃ | 10.30 | 10.37 | 10.58 | 10.66 | 8.96 | 0.04 | 11.23 | 0.22 | 10.01 |
| FeO_r^h | 18.80 | 18.79 | 19.19 | 19.34 | 20.72 | 0.21 | 17.59 | 0.30 | 19.97 |
| MnO | 0.34 | 0.35 | 0.36 | 0.37 | 0.40 | 0.02 | 0.32 | 0.03 | 0.32 |
| MgO | 9.13 | 10.37 | 10.58 | 10.66 | 9.75 | 0.08 | 8.92 | 0.41 | 8.86 |
| CaO | 6.82 | 5.90 | 6.02 | 6.07 | 5.99 | 0.04 | 5.33 | 0.05 | 5.39 |
| Na₂O | 2.86 | 2.62 | 2.68 | 2.70 | 2.33 | 0.28 | 2.09 | 0.17 | 2.07 |
| K₂O | 0.48 | 0.67 | 0.67 | 0.68 | 0.58 | 0.05 | 0.53 | 0.03 | 0.56 |
| P₂O₅ | 0.90 | 0.95 | 0.97 | 0.97 | 0.90 | 0.03 | 0.94 | 0.04 | 0.91 |
| Cr₂O₃ | 0.40 | 0.20 | 0.20 | 0.20 | 0.24 | 0.01 | 0.17 | 0.01 | 0.16 |
| SO₃ | - | 2.32 | 0.76 | 0.00 | 0.02 | 0.01 | 0.61 | 0.13 | 2.38 |
| Cl | - | 0.44 | 0.00 | 0.00 | 0.06 | 0.01 | 2.54 | 0.23 | 1.30 |

931

Table 1. Chemical composition of Martian rock Irvine and EMP analysis of synthetic source glass. ^aHahn and McLennan (2010); ^bMcSween et al. (2006); ^cS- and Cl- free Irvine; ^dnumber of analyses; ^e1 σ standard deviations listed for samples analyzed by EMP; ^fSynthetic Irvine with added Cl and S; ^gI(Cl+S) with added crystalline products from S-rich immiscible melt from high pressure glass synthesis, reported analysis is a weighted average of two immiscible “melts”; ^hall Fe as FeO. Additional data are in supplementary material.

| | |
|-----|-------------------------|
| 932 | No sublimates observed |
| 933 | Sample used for ICP-OES |
| 934 | Sample used for ICP-OES |
| 935 | Sample used for ICP-OES |

Table 2. List of degassing experiments that did not rupture during cooling and experimental products. *experiments containing an additional capsule with oxides used to monitor fO_2 .

934

935

936

| | Element | Fe (ppm) | K (ppm) | Na (ppm) | ^b Total Solid Concentration | ^c Fe/(Na+K) |
|--------------------|------------------------|----------|---------|----------|--|------------------------|
| | ^a λ | 259.94 | 766.49 | 589.59 | | |
| I(Cl+S) mix A21 | Avg | 48.820 | 3.883 | 10.070 | 162.8 | 1.63 |
| | Stddev | 0.268 | 0.044 | 0.098 | | |
| I(Cl+S) gl A40 | ^d Avg | 32.570 | 3.422 | 2.209 | 63.5 | 1.09 |
| | ^d Stddev | 0.055 | 0.014 | 0.010 | | |
| I(Cl+S) mix A24 | Avg | 51.590 | 4.306 | 9.865 | 157.1 | 1.72 |
| | Stddev | 0.227 | 0.025 | 0.020 | | |

937

938 **Table 3.** Cation concentration of dissolved vapor-deposited material measured by OES-ICP.939 ^aemission line wavelength (nm), ^bbased on weight of tube before and after dissolution of vapor
deposits in nitric acid and acid removal, ^ccation molar ratio, ^dbased on triplicate analyses.

| Unreacted Monitor | | | | A22 (I(NVA)) | | | | A21 (I(Cl+S)) | | | |
|---------------------------------|------------------------------------|---------------------------------|------------------------------------|---------------------------------|------------------------------------|---------------------------------|------------------------------------|---------------------------------|------------------------------------|---------------------------------|------------------------------------|
| Ilmenite-Hematite _{ss} | Ulvospinel-Magnetite _{ss} |
| 2 θ | IIm (mol%) | 2 θ | Ulv (mol%) | 2 θ | IIm (mol%) | 2 θ | Ulv (mol%) | 2 θ | IIm (mol%) | 2 θ | Ulv (mol%) |
| 48.97 | 72.5 | 52.98 | 48 | 49.01 | 69 | 53.03 | 43.5 | 49.07 | 61.5 | 53.19 | 29 |
| 53.421 | 71 | 56.47 | 47.5 | 53.44 | 69 | 56.53 | 42.5 | 53.57 | 58 | 56.68 | 28 |
| 61.84 | 70 | 62 | 49.5 | 61.85 | 70 | 62.03 | 47 | 61.96 | 59 | 62.29 | 28 |
| 63.48 | 72.5 | 70.33 | 47 | 63.47 | 74 | 70.37 | 45 | 63.57 | 62 | 73.58 | 31 |
| 70.79 | 72 | 73.29 | 49 | 70.87 | 67.5 | 73.37 | 44 | 70.06 | 57.5 | | |
| | | 74.29 | 48 | | | 74.36 | 44.5 | | | | |
| Avg | 71.6 | 48.2 | Avg. | 69.9 | | 44.4 | | Avg. | 59.6 | Avg. | 29.0 |

940

941 **Table 4.** Inferred compositions of the oxides of the two-oxide oxygen monitor, before and after
942 exposure to the gas of the two sources.

| Location | Age (Ma) | Lava Vol | Lava Mass ^f | Vapor-deposits | Vapor-deposits | Global thickness |
|--------------------------|----------------------------------|----------------------|------------------------|------------------------|------------------------|------------------|
| | | (km ³) | (kg) | mass ^g (kg) | vol (km ³) | (m) |
| Arsia Mons | 10-250 ^a | 3.3E+03 ^a | 9.90E+15 | 1.98E+14 | 49.5 | 3.40E-04 |
| Central Elysium Planitia | 2-250 ^b | 1.7E+05 ^b | 5.10E+17 | 1.02E+16 | 2550 | 0.02 |
| Olympus Mons | 170-250 ^c | 1.4E+06 ^c | 4.20E+18 | 8.40E+16 | 21000 | 0.15 |
| Medusae Fossae Formation | Hesperian/Amazonian ^d | 1.4E+06 ^e | 4.20E+18 | 8.40E+16 | 21000 | 0.15 |

943

944 **Table 5.** Young extrusive rocks identified on the Martian surface, total erupted volumes, and
945 estimated volumes of vapor deposits added to the Martian surface. ^aRichardson et al. (2017), ^bVaucher
et al. (2009), ^cChadwick et al. (2015), ^dKerber and Head (2010), ^eBradley et al. (2002), ^fassuming a
magma density of 3000 kg/m³, ^gassuming a vapor deposit density of 4000 kg/m³

946 **Acknowledgements**

947 We would like to acknowledge the NASA's Mars Fundamental Research Program for providing
948 the funding for this study. We would also like to thank Donald Lindsley for helpful discussions
949 on oxide equilibria, James Quinn for his help with SEM analysis, and the American Museum of
950 Natural History for the use of their electron microprobe. All data obtained in this study and the
951 experimental and analytical methods used are presented within the body of the text and in tables.
952 Physical products of the work are curated by H. Nekvasil and available upon request.

953

954 **References Cited**

955 Africano, F., Van Rompaey, G., Bernard, A., & Le Guern, F. (2002). Deposition of trace
956 elements from high temperature gases of Satsuma-Iwojima volcano. *Earth, Planets and Space*,
957 54, 275-286. doi: 10.1186/BF03353027

958 Andersen, D. J., Lindsley, D. H., & Davidson, P. M. (1993). QUILF: A pascal program to assess
959 equilibria among Fe, Mg, Mn, Ti- oxides, pyroxenes, olivine, and quartz, *Computers and*
960 *Geoscience*, 19, 1333-1350, doi: 10.1016/0098-3004(93)90033-2

961 Argo, J. (1981). On the nature of 'ferrous' corrosion products on marine iron. *Studies in*
962 *Conservation*, 26, 42-44. doi: 10.1179/sic.1981.26.1.42

963 Atreya, S. K., Wong, A. S., Renno, N. O., Farrell, W. M., Delory, G. T., Sentman, D. D., et al.
964 (2006). Oxidant enhancement in martian dust devils and storms: implications for life and
965 habitability. *Astrobiology*, 6, 439-450. doi: 10.1089/ast.2006.6.439

966 Aubaud, C., Hauri, E. H., & Hirschmann, M. M. (2004). Hydrogen partition coefficients between
967 nominally anhydrous minerals and basaltic melts, *Geophysical Research Letters*, 31, doi:
968 10.1029/2004GL021341

969 Baird, A. K., Toulmin, P., Clark, B. C., Rose, H. J., Keil, K., Christian, R. P., & Gooding, J. L.
970 (1976). Mineralogic and petrologic implications of Viking geochemical results from Mars:
971 Interim report. *Science*, 194, 1288-1293.

972 Balta, J. B., Sanborn, M., McSween, H. Y. & Wadhwa, M. (2013). Magmatic history and
973 parental melt composition of olivine-phyric shergottite LAR 06319: Importance of magmatic
974 degassing and olivine antecrysts in martian magmatism. *Meteoritics and Planetary Science*, 48,
975 1359-1382. doi: 10.1111/maps.12140

976 Banin, A., Ben-Shlomo, T., Margulies, L., Blake, D. F., Mancinelli, R. L., & Gehring, A. U.
977 (1993). The nanophase iron mineral(s) in Mars soil. *Journal of Geophysical Research: Planets*,
978 98, 20831-20853. doi: 10.1029/93JE02500

979 Barron, V., & Torrent, J. (2002). Evidence for a simple pathway to maghemite in Earth and Mars
980 soils. *Geochimica et Cosmochimica Acta*, 66, 2801-2806. doi: 10.1016/S0016-7037(02)00876-1

981 Benison, K. C., & LaClair, D. A. (2003). Modern and ancient extremely acid saline deposits:
982 terrestrial analogs for martian environments? *Astrobiology*, 3, 609-618.

983 Benoit, M. H., Nyblade, A. A., & VanDecar, J. C. (2006). Upper mantle P-wave speed variations
984 beneath Ethiopia and the origin of the Afar hotspot. *Geology*, 34(5), 329-332.

985 Berger, J., King, P. L., Spilde, M. N., Wright, S. P., Kunkel, T. S., Lee, R., et al. (2015). Effect
986 of halite coatings on thermal infrared spectra, *Journal of Geophysical Research: Solid Earth*,
987 120(4), 2162-2178. doi: 10.1002/2014JB011712

988 Berger, J. A., Schmidt, M. E., Gellert, R., Campbell, J. L., King, P. L., Flemming, R. L., et al.
989 (2016). A global Mars dust composition refined by the Alpha Particle Xray Spectrometer in Gale
990 Crater. *Geophysical Research Letters*, 43, 67-75. doi: 10.1002/2015GL066675

991 Bernard, A., & Le Guern, F. (1986). Condensation of volatile elements in high-temperature gases
992 of Mount St. Helens. *Journal of Volcanology and Geothermal Research*, 28, 91-105. doi:
993 10.1016/0377-0273(86)90007-7

994 Bertelsen, P., Goetz, W., Madsen, M. B., Kinch, K. M., Hviid, S. F., Knudsen, J. M., & Bell, J.
995 F. (2004). Magnetic properties experiments on the Mars Exploration Rover Spirit at Gusev
996 crater. *Science*, 305, 827-829.

997 Bibring, J. P., Squyres, S. W., & Arvidson, R. E. (2006). Merging views on Mars. *Science*, 1899-
998 1901.

999 Bluth, G. J., Scott, C. J., Sprod, I. E., Schnetzler, C. C., Krueger, A. J., & Walter, L. S. (1995).
1000 Explosive emissions of sulfur dioxide from the 1992 Crater Peak eruptions, Mount Spurr
1001 volcano, Alaska. In: Keith, TEC (ed) The 1992 eruptions of Crater Peak vent, Mount Spurr
1002 volcano, Alaska. *US Geol. Surv. Bull.*, 2139, 37-4.

1003 Bogatyrev, A. F., Makeenkova, O. A., & Nezovitina, M. A. (2014). Temperature and
1004 concentration dependences of thermal-diffusion separation in ternary gas systems. *Journal of
1005 Engineering Physics and Thermophysics*, 87, 1255-1265. doi: 10.1007/s10891-014-1128-8

1006 Bradley, B.A., Sakimoto, S.E.H., Frey, H., Zimbelman, J.R. (2002). Medusae Fossae Formation:

1007 New perspectives from Mars Global Surveyor. *Journal of Geophysical Research*, 107, E8.

1008 Buddington, A. F., & Lindsley, D. H. (1964). Iron-titanium oxide minerals and synthetic

1009 equivalents. *Journal of Petrology*, 5, 310-357. doi: 10.1093/petrology/5.2.310

1010 Burns, R. G., & Fisher, D. S. (1990). Iron-sulfur mineralogy of Mars: Magmatic evolution and

1011 chemical weathering products. *Journal of Geophysical Research*, 95, 14415-14421. doi:

1012 10.1029/JB095iB09p14415

1013 Carrier, B. L., & Kounaves, S. P. (2015). The origins of perchlorate in the martian soil,

1014 *Geophysical Research Letters*, 42, 3739–3745. doi: 10.1002/2015GL064290

1015 Chadwick, J., McGovern, P., Simpson, M., & Reeves, A. (2015). Late Amazonian subsidence

1016 and magmatism of Olympus Mons, Mars. *Journal of Geophysical Research: Planets*, 120, 1585–

1017 1595. doi:10.1002/2015JE004875

1018 Chapman, S., & Dootson, F.W. (1917). XXII. A note on thermal diffusion. *The London,*

1019 *Edinburgh, and Dublin Philosophical Magazine and Journal of Science*, 33, 248-253. doi:

1020 10.1080/14786440308635635

1021 Chapman, S., & Cowling, T. G. (1953). *The Mathematical Theory of Non-uniform Gases: Notes*

1022 *Added in 1951*. Cambridge University Press.

1023 Chase, M.W. Jr. (1998). NIST-JANAF Thermochemical tables 4th ed. J Phys Chem Ref Data

1024 Monograph No 9.

1025 Chevrier, V., & Mathé, P. E. (2007). Mineralogy and evolution of the surface of Mars: a review,

1026 *Planetary and Space Science*, 55, 289-314. doi: 10.1016/j.pss.2006.05.039

1027 Chouinard, A., Williams-Jones, A. E., Leonardson, R. W., Hodgson, C. J., Silva, P., Téllez, C., et
1028 al. (2005). Geology and genesis of the multistage high-sulfidation epithermal Pascua Au-Ag-Cu
1029 deposit, Chile and Argentina. *Economic Geology*, 100, 463-490. doi:
1030 10.2113/gsecongeo.100.3.463

1031 Clark, B.C., Baird, A.K., Rose, H.J., Toulmin, P., Christian, R.P., Kelliher, W.C. et al. (1977).
1032 The Viking X ray fluorescence experiment: Analytical methods and early results. *Journal of*
1033 *Geophysical Research*, 82, 4577-4594. doi: 10.1029/JS082i028p04577

1034 Clark, B. C. & Baird, A. K. (1979). Is the martian lithosphere sulfur rich? *Journal of*
1035 *Geophysical Research*, 84, 8395-8403. doi: 10.1029/JB084iB14p08395

1036 Clark, B. C. & Van Hart, D. C. (1981). The salts of Mars. *Icarus*, 45, 370-378.
1037 doi:10.1016/0019-1035(81)90041-5

1038 Clark, B. C., Baird, A. K., Weldon, R. J., Tsusaki, D. M., Schnabel, L., & Candelaria, M. P.
1039 (1982). Chemical composition of martian fines. *Journal of Geophysical Research*, 87, 10059-
1040 10067. doi: 10.1029/JB087iB12p10059

1041 Cumplido, J., Barrón, V., & Torrent, J. (2000). Effect of phosphate on the formation of
1042 nanophase lepidocrocite from Fe (II) sulfate. *Clays and Clay Minerals*, 48, 503-510.

1043 Dai, Y. D., Yu, Z., Huang, H. B., He, Y., Shao, T., & Hsia, Y. F. (2003). Thermal decomposition
1044 of iron oxychloride as studied by thermal analysis, X-ray diffraction and Mössbauer
1045 spectroscopy. *Materials Chemistry and Physics*, 79, 94-97. doi: 10.1016/S0254-0584(02)00449-2

1046 Deen, W. M. (2013). *Analysis of Transport Phenomena*. Oxford University Press.

1047 Dehouck, E., Chevrier, V., Gaudin, A., Mangold, N., Mathé, P. E., & Rochette, P. (2012).
1048 Evaluating the role of sulfide-weathering in the formation of sulfates or carbonates on Mars.
1049 *Geochimica et Cosmochimica Acta*. 90, 47-63. doi: 10.1016/j.gca.2012.04.057

1050 Delmelle, P., Stix, J., Baxter, P., Garcia-Alvarez, J., & Barquero, J. (2002). Atmospheric
1051 dispersion, environmental effects and potential health hazard associated with the low-altitude gas
1052 plume of Masaya volcano, Nicaragua. *Bulletin of Volcanology*, 64, 423-434. doi:
1053 10.1007/s00445-002-0221-6

1054 de Moor, J. M., Fischer, T. P., Sharp, Z. D., King, P. L., Wilke, M., Botcharnikov, R. E., &
1055 Rivard, C. (2013). Sulfur degassing at Erta Ale (Ethiopia) and Masaya (Nicaragua) volcanoes:
1056 Implications for degassing processes and oxygen fugacities of basaltic systems. *Geochemistry,*
1057 *Geophysics, Geosystems*, 14, 4076-4108.

1058 Dixon, J. E., Stolper, E. M., & Holloway, J. R. (1995). An experimental study of water and
1059 carbon dioxide solubilities in mid-ocean ridge basaltic liquids. Part I: calibration and solubility
1060 models. *Journal of Petrology*, 36, 1607-1631. doi: 10.1093/oxfordjournals.petrology.a037267

1061 Dutrizac, J. E. (2008). Factors affecting the precipitation of potassium jarosite in sulfate and
1062 chloride media. *Metallurgical and Material Transactions B*, 39, 771-783. doi: 10.1007/s11663-
1063 008-9198-7

1064 Erisman, J. W., & Baldocchi, D. (1994). Modelling dry deposition of SO₂. *Tellus B*, 46, 159-
1065 171. doi: 10.1034/j.1600-0889.1994.t01-2-00001.x

1066 Filiberto, J., & Treiman, A. H. (2009). Martian magmas contained abundant chlorine, but little
1067 water. *Geology*, 37, 1087-1090. doi: 10.1130/G30488A.1

1068 Filiberto, J., Baratoux, D., Beaty, D., Breuer, D., Farcy, B. J., Grott, M., et al. (2016a). A review
1069 of volatiles in the martian interior. *Meteoritics & Planetary Science*, 51(11), 1935-1958. doi:
1070 10.1111/maps.12680

1071 Filiberto, J., Gross, J., & McCubbin, F. M. (2016b). Constraints on the water, chlorine, and
1072 fluorine content of the martian mantle. *Meteoritics & Planetary Science*, 51, 2023-2035. doi:
1073 10.1111/maps.12624

1074 Fowler, D., Duyzer, J. H., & Baldocchi, D. D. (1990). Inputs of trace gases, particles and cloud
1075 droplets to terrestrial surfaces. *Proceedings of the Royal Society of Edinburgh, Section B:*
1076 *Biological Sciences*, 97, 35-59. doi: 10.1017/S0269727000005285

1077 Franz, H., King, P.L. & Gaillard, F. (2018). Sulfur on Mars from the atmosphere to the core. In:
1078 Filiberto, J. and Schwenzer, S.P. (eds.), *Volatile in the Martian Crust*, Elsevier, 119-183.

1079 Gaillard, F., & Scaillet, B. (2009). The sulfur content of volcanic gases on Mars. *Earth and*
1080 *Planetary Science Letters*, 279, 34-43. doi: 10.1016/j.epsl.2008.12.028

1081 Gaillard, F., Michalski, J., Berger, G., McLennan, S. M., & Scaillet, B. (2013). Geochemical
1082 reservoirs and timing of sulfur cycling on Mars. *Space Science Reviews*, 174, 251-300. doi:
1083 10.1007/s11214-012-9947-4

1084 Gellert, R., Rieder, R., Anderson, R. C., Brückner, J., Clark, B. C., Dreibus, G., et al. (2004).
1085 Chemistry of rocks and soils in Gusev Crater from the Alpha Particle X-ray Spectrometer,
1086 *Science*, 305, 829-832. doi: 10.1126/science.1099913

1087 Gellert, R., Rieder, R., Brückner, J., Clark, B. C., Dreibus, G., Klingelhöfer, G., et al. (2006).

1088 Alpha particle X-ray spectrometer (APXS): Results from Gusev crater and calibration report,

1089 *Journal of Geophysical Research*, 111. doi: 10.1029/2005JE002555

1090 Ghiorso, M. S., & Sack, R. O. (1995). Chemical mass transfer in magmatic processes IV. A

1091 revised and internally consistent thermodynamic model for the interpolation and extrapolation of

1092 liquid-solid equilibria in magmatic systems at elevated temperatures and pressures.

1093 *Contributions to Mineralogy and Petrology*, 119, 197-212. doi: 10.1007/BF00307281

1094 Gillespie, L. J. (1939). A Simple Theory for Separation of Gases by Thermal Diffusion. *The*

1095 *Journal of Chemical Physics*, 7, 530-535. doi: 10.1063/1.1750482

1096 Glavin, D. P., Freissinet, C., Miller, K. E., Eigenbrode, J. L., Brunner, A. E., Buch, A., et al.

1097 (2013). Evidence for perchlorates and the origin of chlorinated hydrocarbons detected by SAM at

1098 the Rocknest aeolian deposit in Gale Crater. *Journal of Geophysical Research*, 118, 1955-1973.

1099 doi: 10.1002/jgre.20144

1100 Glotch, T. D., Bandfield, J. L., Tornabene, L. L., Jensen, H. B., & Seelos, F. P. (2010).

1101 Distribution and formation of chlorides and phyllosilicates in Terra Sirenum, Mars. *Geophysical*

1102 *Research Letters*, 37. doi: 10.1029/2010GL044557

1103 Glotch, T. D., Bandfield, J. L., Wolff, M. J., Arnold, J. A., & Che, C. (2016). Constraints on the

1104 composition and particle size of chloride salt-bearing deposits on Mars. *Journal of Geophysical*

1105 *Research*, 121, 454-471. doi:10.1002/2015JE004921

1106 Gooding, J. L. (1978). Chemical weathering on Mars thermodynamic stabilities of primary

1107 minerals (and their alteration products) from mafic igneous rocks. *Icarus*, 33(3), 483-513.

1108 Gooding, J. L., Arvidson, R. E., & Zolotov, M. Y. (1992). Physical and chemical weathering. In
1109 *Mars*. University of Arizona Press, Space Science Series.

1110 Gorban, A. N., Sargsyan, H. P., & Wahab, H. A. (2011). Quasichemical models of
1111 multicomponent nonlinear diffusion. *Mathematical Modelling of Natural Phenomena*, 6(5), 184-
1112 262. doi: 10.1051/mmnp/20116509

1113 Gough, R. V., Chevrier, V. F., & Tolbert, M. A. (2014). Formation of aqueous solutions on Mars
1114 via deliquescence of chloride-perchlorate binary mixtures. *Earth and Planetary Science Letters*,
1115 393, 73-82. doi: 10.1016/j.epsl.2014.02.002

1116 Gough, R. V., Chevrier, V. F., & Tolbert, M. A. (2016). Formation of liquid water at low
1117 temperatures via the deliquescence of calcium chloride: Implications for Antarctica and Mars.
1118 *Planetary and Space Science*, 131, 79-87. doi: 10.1016/j.pss.2016.07.006

1119 Hahn, B. C., & McLennan, S. M., (2010). Sediments and the chemical composition of the upper
1120 martian crust. In *First International Conference on Mars Sedimentology and Stratigraphy* (Vol.
1121 1547, p. 30).

1122 Halbert, T. R., Johnston, D. C., McCandlish, L. E., Thompson, A. H., Scanlon, J. C., & Dumesic,
1123 J. A. (1980). Intercalation of organometallic compounds into layered transition metal oxyhalides.
1124 *Physica B+C*, 99, 128-132. doi: 10.1029/2011GL047310

1125 Hauber, E., Brož, P., Jagert, F., Jodłowski, P., & Platz, T. (2011). Very recent and wide-spread
1126 basaltic volcanism on Mars. *Geophysical Research Letters*, 38(10). doi: 10.1029/2011GL047310

1127 Hecht, M. H., Kounaves, S. P., Quinn, R. C., West, S. J., Young, S. M. M., Ming, D. W., et al.
1128 (2009). Detection of perchlorate and the soluble chemistry of martian soil at the Phoenix lander
1129 site. *Science*, 325, 64-67. doi: 10.1126/science.1172466

1130 Herd, C. D., Papike, J. J., & Brearley, A. J. (2001). Oxygen fugacity of martian basalts from
1131 electron microprobe oxygen and TEM-EELS analyses of Fe-Ti oxides. *American Mineralogist*,
1132 86(9), 1015-1024. doi: 10.2138/am-2001-8-908

1133 Herd, C. D. (2006). Insights into the redox history of the NWA 1068/1110 martian basalt from
1134 mineral equilibria and vanadium oxybarometry. *American Mineralogist*, 91(10), 1616-1627. doi:
1135 10.2138/am.2006.2104

1136 Hynek, B. M., Osterloo, M. K., & Kierein-Young, K. S. (2015). Late-stage formation of martian
1137 chloride salts through ponding and evaporation. *Geology*, 43, 787-790. doi: 10.1130/G36895.1

1138 Joachim, B., Pawley, A., Lyon, I. C., Marquardt, K., Henkel, T., Clay, P. L., et al. (2015).
1139 Experimental partitioning of F and Cl between olivine, orthopyroxene and silicate melt at Earth's
1140 mantle conditions. *Chemical Geology*, 416, 65-78. doi: 10.1016/j.chemgeo.2015.08.012

1141 Johnson, M. C., Rutherford, M. J., & Hess, P. C. (1991). Chassigny petrogenesis: Melt
1142 compositions, intensive parameters and water contents of martian (?) magmas. *Geochimica et*
1143 *Cosmochimica Acta*, 55, 349-366. doi: 10.1016/0016-7037(91)90423-3

1144 Johnson, E. R., Wallace, P. J., Cashman, K. V., & Granados, H. D. (2010). Degassing of
1145 volatiles (H₂O, CO₂, S, Cl) during ascent, crystallization, and eruption at mafic monogenetic
1146 volcanoes in central Mexico. *Journal of Volcanology and Geothermal Research*, 197, 225-238.
1147 doi: 10.1016/j.jvolgeores.2010.02.017

1148 Jones, J. H. (2015). Various aspects of the petrogenesis of the martian shergottite meteorites.

1149 *Meteoritics & Planetary Science*, 50(4), 674-690. doi: 10.1111/maps.12421

1150 Jubb, A. M., & Allen, H. C. (2010). Vibrational spectroscopic characterization of hematite,

1151 maghemite, and magnetite thin films produced by vapor deposition. *ACS Applied Materials &*

1152 *Interfaces*, 2, 2804-2812. doi: 10.1021/am1004943

1153 Jugo, J., Wilke, M., & Botcharnikov, R.E. (2010). Sulfur K-edge XANES analysis of natural and

1154 synthetic basaltic glasses: Implications for S speciation and S content as a function of oxygen

1155 fugacity. *Geochimica et Cosmochimica Acta*, 74, 5926–5938.

1156 Kanungo, S. B., & Mishra, S. K. (1997). Kinetics of chloridization of nickel-bearing lateritic iron

1157 ore by hydrogen chloride gas. *Metallurgical and Materials Transactions B*, 28, 389-399, doi:

1158 10.1007/s11663-997-0104-5

1159 Keller, J. M., Boynton, W. V., Karunatillake, S., Baker, V. R., Dohm, J. M., Evans, L. G., et al.

1160 (2006). Equatorial and midlatitude distribution of chlorine measured by Mars Odyssey GRS.

1161 *Journal of Geophysical Research*, 111. doi: 10.1029/2006JE002679

1162 Kerber, L. & Head, J.W. (2010) The age of the Medusae Fossae Formation: Evidence of

1163 Hesperian emplacement from crater morphology, stratigraphy, and ancient lava contacts. *Icarus*,

1164 206, 669–684.

1165 Kiefer, W. S., Filiberto, J., Sandu, C., & Li, Q. (2015). The effects of mantle composition on the

1166 peridotite solidus: Implications for the magmatic history of Mars. *Geochimica et Cosmochimica*

1167 *Acta*, 162, 247-258. doi: 10.1016/j.gca.2015.02.010

1168 King, P. L., Lescinsky, D. T., & Nesbitt, H. W. (2004). The composition and evolution of
1169 primordial solutions on Mars, with application to other planetary bodies. *Geochimica et*
1170 *Cosmochimica Acta*, 68(23), 4993-5008.

1171 King, P. L., & McSween Jr., H. Y. (2005). Effects of H₂O, pH, and oxidation state on the
1172 stability of Fe minerals on Mars. *Journal of Geophysical Research: Planets*, 110(E12). doi:
1173 10.1029/2005JE002482

1174 King, P. L. & McLennan, S. M. (2010). Sulfur on Mars, *Elements*, 6(2), 107-112. doi:
1175 10.2113/gselements.6.2.107

1176 King P.L., Wheeler V.W., Renggli C.J., Palm, A.B., Wilson, S., Harrison, et al. (2018). Gas-
1177 solid reactions: theory, experiments and case studies relevant to Earth and planetary processes.
1178 *Reviews in Mineralogy and Geochemistry*, 84, 1-56.

1179 Korzhinskii, M. A., Tkachenko, S. I., Bulgakov, R. F., & Shmulovich, K. I. (1996). Condensate
1180 compositions and native metals in sublimes of high-temperature gas streams of Kudryavyi
1181 Volcano, Iturup Island, Kuril Islands. *Geochemistry International C/C of Geokhimica*, 34, 1057-
1182 1064.

1183 Kounaves, S. P., Carrier, B. L., O'Neil, G. D., Stroble, S. T., & Claire, M. W. (2014). Evidence
1184 of martian perchlorate, chlorate, and nitrate in Mars meteorite EETA79001: Implications for
1185 oxidants and organics. *Icarus*, 229, 206-213. doi: 10.1016/j.icarus.2013.11.012

1186 Krauskopf, K.B. (1957). The heavy metal content of magmatic vapor at 600°C, *Economic*
1187 *Geology*, 52, 786-807. doi: 10.2113/gsecongeo.52.7.786

1188 Krauskopf, K.B. (1964). The possible role of volatile metal compounds in ore genesis. *Economic*
1189 *Geology*, 59, 22-45. doi: 10.2113/gsecongeo.59.1.22

1190 Kulshrestha, M. J., Kulshrestha, U. C., Parashar, D. C., & Vairamani, M. (2003). Estimation of
1191 SO₄ contribution by dry deposition of SO₂ onto the dust particles in India. *Atmospheric*
1192 *Environment*, 37, 3057-3063. doi: 10.1016/S1352-2310(03)00290-5

1193 Lammer, H., Chassefière, E., Karatekin, Ö., Morschhauser, A., Niles, P. B., Mousis, O., et al.
1194 (2013). Outgassing history and escape of the martian atmosphere and water inventory. *Space*
1195 *Science Reviews*, 174, 113-154. doi: 10.1007/s11214-012-9943-8

1196 Leshin, L. A., Epstein, S., & Stolper, E. M. (1996). Hydrogen isotope geochemistry of SNC
1197 meteorites. *Geochimica et Cosmochimica Acta*, 60, 2635-2650. doi: 10.1016/0016-
1198 7037(96)00122-6

1199 Leshin, L. A., Mahaffy, P. R., Webster, C. R., Cabane, M., Coll, P., Conrad, P. G., et al. (2013).
1200 Volatile, isotope, and organic analysis of martian fines with the Mars Curiosity rover. *Science*,
1201 341, 1238937. doi: 10.1126/science.1238937

1202 Lindsley, D.H. (1976). The crystal chemistry and structure of oxide minerals as exemplified by
1203 the Fe-Ti oxides, and Experimental studies of oxide minerals. *Oxide minerals*.

1204 Madsen, M. B., Hviid, S. F., Gunnlaugsson, H. P., Knudsen, J. M., Goetz, W., Pedersen, C. T., et
1205 al. (1999). The magnetic properties experiments on Mars Pathfinder. *Journal of Geophysical*
1206 *Research: Planets*, 104, 8761-8779. doi: 10.1029/1998JE900006

1207 Mandeville, C. W., Webster, J. D., Rutherford, M. J., Taylor, B. E., Timbal, A., & Faure, K.

1208 (2002). Determination of molar absorptivities for infrared absorption bands of H₂O in andesitic

1209 glasses. *American Mineralogist*, 87, 813-821. doi: 10.2138/am-2002-0702

1210 Mangold, N., Loizeau, D., Poulet, F., Ansan, V., Baratoux, D., LeMouelic, S., et al. (2010).

1211 Mineralogy of recent volcanic plains in the Tharsis region, Mars, and implications for platy-

1212 ridged flow composition. *Earth and Planetary Science Letters*, 294, 440-450. doi:

1213 10.1016/j.epsl.2009.07.036

1214 Massé, M., Bourgeois, O., Le Mouélic, S., Verpoorter, C., Le Deit, L., & Bibring, J. P. (2010).

1215 Martian polar and circum-polar sulfate-bearing deposits: Sublimation tills derived from the

1216 North Polar Cap. *Icarus*, 209, 434-451. doi: 10.1016/j.icarus.2010.04.017

1217 Mather, T. A., Allen, A. G., Oppenheimer, C., Pyle, D. M., & McGonigle, A. J. S. (2003). Size-

1218 resolved characterisation of soluble ions in the particles in the tropospheric plume of Masaya

1219 volcano, Nicaragua: Origins and plume processing. *Journal of Atmospheric Chemistry*, 46, 207-

1220 237. doi: 10.1023/A:102632750

1221 McCollom, T. M., & Hynek, B. M. (2005). A volcanic environment for bedrock diagenesis at

1222 Meridiani Planum on Mars. *Nature*, 438, 1129. doi: 10.1038/nature04390

1223 McCubbin, F. M., & Nekvasil, H. (2008). Maskelynite-hosted apatite in the Chassigny meteorite:

1224 Insights into late-stage magmatic volatile evolution in martian magmas. *American Mineralogist*,

1225 93, 676-684. doi: 10.2138/am.2008.2558

1226 McCubbin, F. M., Tosca, N. J., Smirnov, A., Nekvasil, H., Steele, A., Fries, M., et al. (2009).

1227 Hydrothermal jarosite and hematite in a pyroxene-hosted melt inclusion in martian meteorite

1228 MIL 03346: Implications for magmatic hydrothermal fluids on Mars. *Geochimica et*
1229 *Cosmochimica Acta*, 73, 4907-4917. doi: 10.1016/j.gca.2009.05.031

1230 McCubbin, F. M., Smirnov, A., Nekvasil, H., Wang, J., Hauri, E., & Lindsley, D. H. (2010).
1231 Hydrous magmatism on Mars: A source of water for the surface and subsurface during the
1232 Amazonian. *Earth and Planetary Science Letters*, 292, 132-138. doi: 10.1016/j.epsl.2010.01.028

1233 McCubbin, F. M., Hauri, E. H., Elardo, S. M., Vander Kaaden, K. E., Wang, J., & Shearer, C. K.
1234 (2012). Hydrous melting of the martian mantle produced both depleted and enriched shergottites,
1235 *Geology*, 40, 683-686. doi: 10.1130/G33242.1

1236 McCubbin, F. M., Boyce, J. W., Novák-Szabó, T., Santos, A. R., Tartèse, R., Muttik, N., et al.
1237 (2016). Geologic history of martian regolith breccia Northwest Africa 7034: Evidence for
1238 hydrothermal activity and lithologic diversity in the martian crust. *Journal of Geophysical*
1239 *Research: Planets*, 121, 2120-2149. doi: 10.1002/2016JE005143

1240 McLennan, S.M., Anderson, R.B., Bell III, J.F., Bridges, J.C., Calef III, F., Campbell, J.L., et al.
1241 (2014). Elemental Geochemistry of Sedimentary Rocks in Yellowknife Bay, Gale Crater, Mars.
1242 *Science*, doi:10.1126/science.1244734.

1243 McLennan, S. M., Bell III, J. F., Calvin, W. M., Christensen, P. R., Clark, B. D., De Souza, P.
1244 A., et al. (2005). Provenance and diagenesis of the evaporite-bearing Burns formation, Meridiani
1245 Planum, Mars. *Earth and Planetary Science Letters*, 240, 95-121. doi:
1246 10.1016/j.epsl.2005.09.041

1247 McSween, H. Y. & Harvey, R. P. (1993). Outgassed water on Mars: Constraints from melt
1248 inclusions in SNC meteorites. *Science*, 259, 1890-1892. doi: 10.1126/science.259.5103.1890

1249 McSween, H. Y. (1994). What we have learned about Mars from SNC meteorites. *Meteoritics*
1250 and *Planetary Science*, 29, 757-779. doi: 10.1111/j.1945-5100.1994.tb01092.x

1251 McSween, H. Y., Wyatt, M. B., Gellert, R., Bell, J. F., Morris, R. V., Herkenhoff, K. E., et al.
1252 (2006). Characterization and petrologic interpretation of olivine-rich basalts at Gusev Crater,
1253 Mars. *Journal of Geophysical Research*, 111, E2. doi: 10.1029/2005JE002477

1254 Mège, D. & Masson, P. (1996). A plume tectonics model for the Tharsis province, Mars,
1255 *Planetary and Space Science*, 44, 1499-1546. doi: 10.1016/S0032-0633(96)00113-4

1256 Meslin, P. Y., Gasnault, O., Forni, O., Schröder, S., Cousin, A., Berger, G., et al. (2013). Soil
1257 diversity and hydration as observed by ChemCam at Gale Crater, Mars. *Science*, 341, 1238670.
1258 doi: 10.1126/science.1238670

1259 Ming, D. W., Archer, P. D., Glavin, D. P., Eigenbrode, J. L., Franz, H. B., Sutter, B., et al.
1260 (2014). Volatile and organic compositions of sedimentary rocks in Yellowknife Bay, Gale
1261 Crater, Mars. *Science*, 343, 1245267. doi: 10.1126/science.1245267

1262 Morris, R. V., Golden, D. C., Sheller, T. D., & Lauer, H. V. (1998). Lepidocrocite to maghemite
1263 to hematite: a pathway to magnetic and hematitic martian soil. *Meteoritics and Planetary*
1264 *Science*, 33, 743-751. doi: 10.1111/j.1945-5100.1998.tb01680.x

1265 Morris, R. V., Golden, D. C., Bell, J. F., Sheller, T. D., Scheinost, A. C., Hinman, N. W., et al.
1266 (2000). Mineralogy, composition, and alteration of Mars Pathfinder rocks and soils: Evidence
1267 from multispectral, elemental, and magnetic data on terrestrial analogue, SNC meteorite, and
1268 Pathfinder samples. *Journal of Geophysical Research: Planets*, 105(E1), 1757-1817. doi:
1269 10.1029/1999JE001059

1270 Morris, R. V., Golden, D. C., Ming, D. W., Shelper, T. D., Jørgensen, L. C., Bell, J. F., et al.
1271 (2001). Phyllosilicate-poor palagonitic dust from Mauna Kea Volcano (Hawaii): A mineralogical
1272 analogue for magnetic martian dust? *Journal of Geophysical Research: Planets*, *106*, 5057-5083.
1273 doi: 10.1029/2000JE001328

1274 Morris, R. V., Klingelhoefer, G., Schröder, C., Rodionov, D. S., Yen, A., Ming, D. W., et al.
1275 (2006). Mössbauer mineralogy of rock, soil, and dust at Gusev crater, Mars: Spirit's journey
1276 through weakly altered olivine basalt on the plains and pervasively altered basalt in the Columbia
1277 Hills, *Journal of Geophysical Research*, *111*,. doi: 10.1029/2005JE002584

1278 Nachon, M., Clegg, S. M., Mangold, N., Schröder, S., Kah, L. C., Dromart, G., et al. (2014).
1279 Calcium sulfate veins characterized by ChemCam/Curiosity at Gale crater, Mars. *Journal of
1280 Geophysical Research: Planets*, *119*, 1991-2016. doi: 10.1002/2013JE004588

1281 Navrotksy, A., Forray, F. L., & Drouet, C. (2005). Jarosite stability on Mars. *Icarus*, *176*, 250-
1282 253. doi: 10.1016/j.icarus.2005.02.003

1283 Nekvasil, H., Dondolini, A., Horn, J., Filiberto, J., Long, H., & Lindsley, D. H. (2004). The
1284 origin and evolution of silica-saturated alkalic suites: An experimental study. *Journal of
1285 Petrology*, *45*, 693-721. doi: 10.1093/petrology/egg103

1286 Niles, P. B., & Michalski, J. (2009). Meridiani Planum sediments on Mars formed through
1287 weathering in massive ice deposits. *Nature Geoscience*, *2*, 215. doi: 10.1038/ngeo438

1288 Nuding, D. L., Rivera-Valentin, E. G., Davis, R. D., Gough, R. V., Chevrier, V. F., & Tolbert,
1289 M. A. (2014). Deliquescence and efflorescence of calcium perchlorate: an investigation of stable
1290 aqueous solutions relevant to Mars. *Icarus*, *243*, 420-428. doi: 10.1016/j.icarus.2014.08.036

1291 Ojha, L., Lewis, K., Karunatillake, S. & Schmidt, M. (2018). The Medusae Fossae Formation as
1292 the single largest source of dust on Mars. *Nature Communications*, 9,:2867. doi:
1293 10.1038/s41467-018-05291-5

1294 Osterloo, M. M., Hamilton, V. E., Bandfield, J. L., Glotch, T. D., Baldridge, A. M., Christensen,
1295 et al. (2008). Chloride-bearing materials in the southern highlands of Mars, *Science*, 319, 1651-
1296 1654. doi: 10.1126/science.1150690

1297 Osterloo, M. M., Anderson, F. S., Hamilton, V. E., & Hynek, B. M. (2010). Geologic context of
1298 proposed chloride-bearing materials on Mars, *Journal of Geophysical Research*, 115. doi:
1299 10.1029/2010JE003613

1300 Patrick, M. R., Dehn, J., & Dean, K. (2004). Numerical modeling of lava flow cooling applied to
1301 the 1997 Okmok eruption: Approach and analysis. *Journal of Geophysical Research: Solid*
1302 *Earth*, 109. doi:10.1029/2003JB002537

1303 Platten, J. K. (2006). The Soret effect: a review of recent experimental results. *Journal of*
1304 *Applied Mechanics*, 73(1), 5-15. doi: 10.1115/1.1992517

1305 Plescia, J. B. (1993). An assessment of volatile release from recent volcanism in Elysium, Mars.
1306 *Icarus*, 104, 20-32. doi: 10.1006/icar.1993.1079

1307 Pokrovski, G. S., Borisova, A.Y., & Bychkov, A.Y. (2013). Speciation and Transport of Metals
1308 and Metalloids in Geological Vapors. *Reviews in Mineralogy and Geochemistry*, 76, 165-218.
1309 doi: 10.2138/rmg.2013.76.6

1310 Renggli, C. J., King, P. L., Henley, R. W., & Norman, M. D. (2017). Volcanic gas composition,
1311 metal dispersion and deposition during explosive volcanic eruptions on the Moon. *Geochimica et*
1312 *Cosmochimica Acta*, 206, 296-311. doi: 10.1016/j.gca.2017.03.012

1313 Righter, K., Dyar, M. D., Delaney, J. S., Vennemann, T. W., Hervig, R. L., & King, P. L. (2002).
1314 Correlations of octahedral cations with OH⁻, O₂⁻, Cl⁻, and F⁻ in biotite from volcanic rocks
1315 and xenoliths. *American Mineralogist*, 87(1), 142-153. doi: 10.2138/am-2002-0115

1316 Robie, R.A., Hemingway, S., & Fisher, J.R. (1979). Thermodynamic Properties of Minerals and
1317 Related Substances at 298.15 K and 1 Bar (105 Pascals) Pressure and at Higher Temperatures.
1318 *U.S. Geological Survey Bulletin*, 1452, pp.464.

1319 Salazar, J.S., Perez, L., de Abril, O., Truong Phuoc, L., Ihiawakrim, D., Vazquez, M., et al.
1320 (2011). Magnetic iron oxide nanoparticles in 10– 40 nm range: composition in terms of
1321 magnetite/maghemite ratio and effect on the magnetic properties. *Chemistry of Materials*, 23,
1322 1379-1386. doi: 10.1021/cm103188a

1323 Santos, A. R., Agee, C. B., McCubbin, F. M., Shearer, C. K., Burger, P. V., Tartese, R., et al.
1324 (2015). Petrology of igneous clasts in Northwest Africa 7034: Implications for the petrologic
1325 diversity of the martian crust. *Geochimica et Cosmochimica Acta*, 157, 56-85. doi:
1326 10.1016/j.gca.2015.02.023

1327 Sautter, V., Jambon, A., & Boudouma, O. (2006). Cl-amphibole in the nakhlite MIL 03346:
1328 Evidence for sediment contamination in a martian meteorite. *Earth and Planetary Science*
1329 *Letters*, 252, 45-55. doi: 10.1016/j.epsl.2006.09.024

1330 Savijärvi, H. I., Harri, A. M., & Kemppinen, O. (2015). Mars Science Laboratory diurnal
1331 moisture observations and column simulations. *Journal of Geophysical Research: Planets*, 120,
1332 1011-1021. doi: 10.1002/2014JE004732

1333 Schmidt, M. E., Schrader, C. M., & McCoy, T. J. (2013). The primary fO₂ of basalts examined
1334 by the Spirit rover in Gusev Crater, Mars: Evidence for multiple redox states in the martian
1335 interior. *Earth and Planetary Science Letters*, 384, 198-208. doi: 10.1016/j.epsl.2013.10.005

1336 Shuttlefield, J. D., Sambur, J. B., Gelwicks, M., Eggleston, C. M., & Parkinson, B. A. (2011).
1337 Photooxidation of chloride by oxide minerals: Implications for perchlorate on Mars. *Journal of*
1338 *American Chemical Society*, 133, 17,521–17,523. doi:10.1021/ja2064878

1339 Sklute, E. C., Rogers, A. D., Gregerson, J. C., Jensen, H. B., Reeder, R. J., & Dyar, M. D.
1340 (2018). Amorphous salts formed from rapid dehydration of multicomponent chloride and ferric
1341 sulfate brines: Implications for Mars. *Icarus*, 302, 285-295. doi: 10.1016/j.icarus.2017.11.018

1342 Settle, M. (1979). Formation and deposition of volcanic sulfate aerosols on Mars. *Journal of*
1343 *Geophysical Research*, 84, 8343-8354. doi: 10.1029/JB084iB14p08343

1344 Shmulovich, K. I. & Churakov, S. V. (1998). Natural fluid phases at high temperatures and low
1345 pressures. *Journal of Geochemical Exploration*, 62, 183-191. doi: 10.1016/S0375-
1346 6742(97)00041-1

1347 Stoffregen, R. E. (1987). Genesis of acid-sulfate alteration and Au-Cu-Ag mineralization at
1348 Summitville, Colorado. *Economic Geology*, 82, 1575-1591. doi: 10.2113/gsecongeo.82.6.1575

1349 Sutter, B., Quinn, R. C., Archer, P. D., Glavin, D. P., Glotch, T. D., Kounaves, S. P., & Ming, D.

1350 W. (2017). Measurements of oxychlorine species on Mars. *International Journal of*

1351 *Astrobiology*, 16, 203-217.

1352 Symonds, R. B. & Reed, M. H. (1993). Calculation of multicomponent chemical equilibria in

1353 gas-solid-liquid systems: Calculation methods, thermochemical data, and applications to studies

1354 of high-temperature volcanic gases with examples from Mt. St. Helens. *American Journal of*

1355 *Science*, 293. doi: 10.2475/ajs.293.8.758

1356 Symonds, R. B., Rose, W. I., Bluth, G. J., & Gerlach, T. M. (1994). Volcanic-gas studies;

1357 methods, results, and applications. *Reviews in Mineralogy and Geochemistry*, 30(1), 1-66.

1358 Taran, Y. A., Hedenquist, J. W., Korzhinsky, M. A., Tkachenko, S. I., & Shmulovich, K. I.

1359 (1995). Geochemistry of magmatic gases from Kudryavy volcano, Iturup, Kuril Islands.

1360 *Geochimica et Cosmochimica Acta*, 59, 1749-1761. doi: 10.1016/0016-7037(95)00079-F

1361 Taran, Y. A., Bernard, A., Gavilanes, J. C., & Africano, F. (2000). Native gold in mineral

1362 precipitates from high-temperature volcanic gases of Colima volcano, Mexico. *Applied*

1363 *Geochemistry*, 15, 337-346. doi: 10.1016/S0883-2927(99)00052-9

1364 Taylor, L. A., Nazarov, M. A., Shearer, C. K., McSween, H. Y., Cahill, J., Neal, C. R., et al.

1365 (2002). Martian meteorite Dhofar 019: A new shergottite. *Meteoritics and Planetary Science*, 37,

1366 1107-1128. doi: 10.1111/j.1945-5100.2002.tb00881.x

1367 Torrent, J. & Barrón, V. (2000). Key role of phosphorus in the formation of the iron oxides in

1368 Mars soils? *Icarus*, 145, 645-647. doi: 10.1006/icar.2000.6408

1369 Ustunisik, G., Nekvasil, H., & Lindsley, D. (2011). Letter. Differential degassing of H₂O, Cl, F,
1370 and S: Potential effects on lunar apatite. *American Mineralogist*, 96, 1650-1653. doi:
1371 10.2138/am.2011.3851

1372 Ustunisik, G., Nekvasil, H., Lindsley, D. H., & McCubbin, F. M. (2015). Degassing pathways of
1373 Cl-, F-, H-, and S-bearing magmas near the lunar surface: Implications for the composition and
1374 Cl isotopic values of lunar apatite. *American Mineralogist*, 100, 1717-1727. doi: 10.2138/am-
1375 2015-4883

1376 Usui, T., Alexander, C. M. D., Wang, J., Simon, J. I., & Jones, J. H. (2012). Origin of water and
1377 mantle–crust interactions on Mars inferred from hydrogen isotopes and volatile element
1378 abundances of olivine-hosted melt inclusions of primitive shergottites. *Earth and Planetary
1379 Science Letters*, 357, 119-129. doi: 10.1016/j.epsl.2012.09.008

1380 Vaniman, D. T., Bish, D.L., Ming, D.W. et al. (2014). Mineralogy of a Mudstone at Yellowknife
1381 Bay, Gale Crater, Mars. *Science*, 343, 1243480-1-1243480-8.

1382 Vaucher, J., Baratoux, D., Mangold, N., Pinet, P., Kurita, K., & Grégoire, M. (2009). The
1383 volcanic history of central Elysium Planitia: Implications for martian magmatism. *Icarus*, 204,
1384 418-442. doi: 10.1016/j.icarus.2009.06.032

1385 Wadhwa, M. (2008). Redox conditions on small bodies, the Moon and Mars. *Reviews in
1386 Mineralogy and Geochemistry*, 68, 493-510. doi: 10.2138/rmg.2008.68.17

1387 Wahrenberger, C. (2002). Volatile trace-element transport in high-temperature gases from
1388 Kudriavy volcano (Itup, Kurile Islands, Russia). *Geochem. Soc., Spec. Publ.*, 7, 307-327.

1389 Wallace, P. J. (2001). Volcanic SO₂ emissions and the abundance and distribution of exsolved
1390 gas in magma bodies. *Journal of Volcanology and Geothermal Research*, 108, 85-106. doi:
1391 10.1016/S0377-0273(00)00279-1

1392 Wänke, H., Dreibus, G., & Wright, I. P. (1994). Chemistry and accretion history of Mars [and
1393 discussion]. *Philosophical Transactions of the Royal Society A*, 349, 285-293. doi:
1394 10.1098/rsta.1994.0132

1395 Wänke, H., Brückner, J., Dreibus, G., Rieder, R., & Ryabchikov, I. (2001). Chemical
1396 composition of rocks and soils at the Pathfinder site. *Space Science Reviews*, 96(1-4), 317-330.
1397 doi: /10.1023/A:1011961725645

1398 Waters, L. E., & Lange, R. A. (2016). No effect of H₂O degassing on the oxidation state of
1399 magmatic liquids. *Earth and Planetary Science Letters*, 447, 48-59. doi:
1400 10.1016/j.epsl.2016.04.030

1401 Watson, L. L., Hutcheon, I. D., Epstein, S., & Stolper, E. M. (1994). Water on Mars: Clues from
1402 deuterium/hydrogen and water contents of hydrous phases in SNC meteorites. *Science*, 265, 86-
1403 90. doi: 10.1126/science.265.5168.86

1404 Webster, A. H., & Bright, N. F. (1961). The System Iron–Titanium–Oxygen at 1200°C and
1405 Oxygen Partial Pressures Between 1 Atm. and 2×10^{-14} Atm. *Journal of the American Ceramic
1406 Society*, 44, 110-116. doi: 10.1111/j.1151-2916.1961.tb13723.x

1407 Weiss, B. P., Vali, H., Baudenbacher, F. J., Kirschvink, J. L., Stewart, S. T., & Shuster, D. L.
1408 (2002). Records of an ancient martian magnetic field in ALH84001. *Earth and Planetary
1409 Science Letters*, 201, 449 -463. doi: 10.1016/S0012-821X(02)00728-8

1410 Whitaker, M. L., Nekvasil, H., Lindsley, D. H., & DiFrancesco, N. J. (2006). The role of
1411 pressure in producing compositional diversity in intraplate basaltic magmas. *Journal of*
1412 *Petrology*, 48, 365-393. doi: 10.1093/petrology/egl063

1413 Wilson, E. H., Atreya, S. K., Kaiser, R. I., & Mahaffy, P. R. (2016). Perchlorate formation on
1414 Mars through surface radiolysis-initiated atmospheric chemistry: A potential mechanism,
1415 *Journal of Geophysical Research*, 121, 1472-1487. doi: 10.1002/2016JE005078

1416 Yang, X. J., Xu, X. M., Xu, J., & Han, Y. F. (2013). Iron oxychloride (FeOCl): an efficient
1417 Fenton-like catalyst for producing hydroxyl radicals in degradation of organic contaminants.
1418 *Journal of the American Chemical Society*, 135, 16058-16061. doi: 10.1021/ja409130c

1419 Yant, M., Rogers, A. D., Nekvasil, H., Zhao, Y. Y. S., & Bristow, T. (2016). Spectral
1420 characterization of acid weathering products on martian basaltic glass. *Journal of Geophysical*
1421 *Research: Planets*, 121, 516-541. doi: 10.1002/2015JE004969

1422 Yudovskaya, M. A., Tessalina, S., Distler, V. V., Chaplygin, I. V., Chugaev, A. V., & Dikov, Y.
1423 P. (2008). Behavior of highly-siderophile elements during magma degassing: A case study at the
1424 Kudryavy volcano. *Chemical Geology*, 248, 318-341. doi: 10.1016/j.chemgeo.2007.12.008

1425 Zelenski, M. E., Fischer, T. P., De Moor, J. M., Marty, B., Zimmermann, L., Ayalew, D., &
1426 Karandashev, V. K. (2013). Trace elements in the gas emissions from the Erta Ale volcano, Afar,
1427 Ethiopia. *Chemical Geology*, 357, 95-116.

1428 Zent, A. P., & McKay, C. P. (1994). The chemical reactivity of the martian soil and implications
1429 for future missions. *Icarus*, 108(1), 146-157.

1430 Zhang, X., Zhuang, G., Chen, J., Wang, Y., Wang, X., An, Z., & Zhang, P. (2006).

1431 Heterogeneous reactions of sulfur dioxide on typical mineral particles. *The Journal of Physical*
1432 *Chemistry B*, 110, 12588-12596. doi: 10.1021/jp0617773

1433 Zhang, J., Liu, G., Wang, P., & Liu, S. (2017). Facile synthesis of FeOCl/iron hydroxide hybrid
1434 nanosheets: enhanced catalytic activity as a Fenton-like catalyst. *New Journal of Chemistry*, 41,
1435 10339-10346. doi: 10.1039/C7NJ01993A

1436 Zolotov, M. Y., and E. L. Shock (2005). Formation of jarosite-bearing deposits through aqueous
1437 oxidation of pyrite at Meridiani Planum, Mars. *Geophysical Research Letters*, 32, L21203.
1438 doi:10.1029/2005GL024253

1439

1440

1441

1442 **Plain Language Summary**

1443 The surface of Mars is covered by dust and will be the most abundant material encountered by
1444 future manned missions to the planet. Understanding the mineralogic makeup of this dust is vital
1445 to assess its potential toxicity. This dust also records information on the most recent geological
1446 activity and atmospheric conditions on Mars. This work focuses on the potential contribution of
1447 micron-sized particles formed by condensation of gas from young lava flows to the dust. We
1448 experimentally simulated a boiling magma and exposed the gas given off to the temperatures that
1449 you might see above a lava flow. The results indicate that some of the minerals found in the fine-
1450 grained material of the martian surface such as chlorides, sulfides, sulfur, and silica could be

1451 formed in this way. These precipitated minerals, in turn, can react with the cooling gas or the
1452 atmosphere to form a set of secondary minerals, such as maghemite and hematite, and very
1453 reactive substances such as iron oxychloride. Iron oxychloride can obliterate traces of organic
1454 material that we have counted on to provide information about organics brought to Mars by
1455 meteorites and about potential past life on the planet.